Modelling secondary circulations in stratified bi-directional flows: A potential mechanism for flux transfer from lower to upper fluid layers

Manel Grifoll [a],[*], Jarle Berntsen [b], Alan Cuthbertson [c]

[a] Department of Civil and Environmental Engineering, Universitat Politècnica de Catalunya (UPC-BarcelonaTech), Barcelona, Catalonia, Spain
[b] Department of Mathematics, University of Bergen, Bergen, Norway
[c] School of Science and Engineering (Civil Engineering), University of Dundee, Dundee, Scotland, UK.

ARTICLE INFO

ABSTRACT

Results are presented for new laboratory-scale numerical simulations of bi-directional stratified flows generated within an idealized trapezoidal sill-channel topography, focussing on the lateral (or secondary) flow structure across the channel both in non-rotating and rotating frames of reference. The simulations utilise the non-hydrostatic Bergen Ocean Model (BOM), a three-dimensional general ocean circulation model. The results from the BOM simulations are verified by large-scale experimental data obtained in the LEGI Coriolis rotating platform in Grenoble, within which velocity and density fields for bi-directional stratified flows were measured through particle image velocimetry (PIV) and micro-conductivity density probes, respectively. The BOM simulations reproduce the main dynamic flow patterns and structure of the large-scale exchange flows generated through the trapezoidal sill-channel, with the lower layer saline intrusion flux shown to reduce, due to partial blockage, as the upper freshwater flow is increased (i.e. net barotropic forcing). Non-rotational BOM simulations show upward (and downward) flow along the centreline of the trapezoidal sill-channel in the upper (and lower) layers, with symmetrical counter-rotating circulation cells forming both above and below the density interface. By contrast, equivalent BOM simulations within a rotating frame of reference show the secondary flow circulation in the lower dense water layer to be dominated by Ekman dynamics, while two co-rotating cells are formed in the upper freshwater layer above the inclined density interface. In these rotational cases, significant upward and downward velocities (i.e. strong upwelling and downwelling) are generated adjacent to the inclined sill-channel side walls (in comparison to non-rotating cases). This secondary flow effect may be especially relevant for exchange flows in estuaries, fjords, deep-ocean channels and sea straits, where the channel width exceeds the Rossby radius of deformation and, thus, Earth rotation effects become important dynamically. In particular, any potential vertical transport pathway associated with this upwelling and downwelling at the inclined channel side slopes may have strong managerial implications in coastal areas, whereby tracers (e.g. contaminants, salinity, reduced DO waters, fine sediments) can be transferred from deep waters to the near surface.

1. Introduction

The analysis of bi-directional stratified flows that are constrained by submerged topography (i.e. channels and sills) has attracted much attention from researchers due both to the complexity of flow dynamics involved and their importance across a wide range of spatial scales, from large-scale global oceanic circulations to more localised estuarine or fjordic circulations. Many past studies encompass different analytical perspectives of the exchange flow dynamics that are often investigated via laboratory scale experiments, reduced and full scale numerical simulations, and/or analysis of observational field data. These studies have often focused on simulating or measuring the Earth's rotational effects (i.e. due to Coriolis forces) on these exchange flows, particularly when passing through a hydraulically-constrained region caused by natural topographic constrictions. As an example, the Faroe-Shetland and Faroe Bank Channel system, which transports approximately one third of the total deep water outflow volume flux that crosses the Greenland-Scotland ridge, has been studied extensively through field data observations (e.g. Johnson and Sandford, 1992; Borenäs and Lundberg, 2004), laboratory scale rotating tank experiments (e.g.

Davies et al., 2006; Cuthbertson et al., 2014) and numerical simulations (e.g. Seim et al., 2010; Stashchuk et al., 2011; Broadbridge and Toumi, 2015). Similarly, rotational effects on the density-driven exchange flow through the Gibraltar strait has been widely investigated using numerical modelling (Papadakis et al., 2003), observational data (Bryden et al., 1994) and laboratory experiments (Davies et al., 2002).

At smaller, more localised spatial scales, the presence of shallow submerged sill, for example at the entrance to a fjord, can initiate partial blockage of tidal intrusions into the semi-enclosed fjordic basin, with a consequential suppression of deep basin water renewal events (Inall et al., 2004). As highlighted by Chant (2010), even at these smaller scales [O(few km)], the effects of the Earth's rotation may be relevant to stratified exchange flow dynamics in such regions of restricted exchange, as characterised by titling of the density interface between the counterflowing fluid layers and induced lateral circulations (e.g. Cerralbo et al., 2015; Chant, 1997; Lerczak and Geyer, 2004; Ott et al., 2002). When these submerged sills (or channels) are relatively wide in comparison to the internal Rossby radius of deformation, Coriolis forces are expected to introduce geostrophic adjustment of the internal fluid motions, exercising a significant influence on the distribution of the density and velocity fields (e.g. Cuthbertson et al., 2021; De Falco et al., 2021; Johnson and Ohlsen, 1994).

In parallel to the collection and analysis of observational data for real exchange flow cases, idealised experimental studies have been conducted in rotating tank and basin facilities to investigate geostrophic adjustment of uni- and bi-directional stratified flows through topographically-constrained channels. For instance, Johnson and Ohlsen (1994) and Rabe et al. (2007) presented results from rotating exchange flow experiments in simple channel geometries with a horizontal constriction. De Falco et al. (2021) investigated exchange flows generated through a rotating, trapezoidal sill-channel, investigating the parametric conditions under which partial blockage of the lower saline water intrusion occurred due to the combined effect of Coriolis accelerations and a strong net-barotropic flow in the upper freshwater layer. Further, when investigating bi-directional stratified flows within a non-rotating frame of reference, Cuthbertson et al. (2018) identified the full blockage conditions for the saline intrusion across a rectangular submerged sill, based on the strength of the upper freshwater flow and the sill submergence depth.

The numerical modelling of geophysical exchange flows for relatively simple channel geometries (e.g. Berntsen et al., 2009; 2016), has also provided a robust alternative approach to simulate these laboratory-scale exchange flows, generally showing a good agreement with measured data on density and velocity fields. In particular, Cuthbertson et al. (2021) investigated numerically bi-directional stratified flows over a rectangular sill section under both non-rotational and rotational frames of reference. This model was validated by the laboratory data obtained for the same sill topography and external forcing conditions, as presented in Cuthbertson et al. (2018). Within the numerical model simulations, the range of parametric conditions was extended beyond the limited number of (non-rotating) physical modelling cases to provide greater insight into the rotating exchange flows dynamics across the sill and the combined effect of net-barotropic flows, sill submergence depth and Coriolis forces on the blockage of saline intrusions across the sill.

Within this rotating frame of reference, the cross-channel secondary flow circulations in stratified flows have also been a focus of interest, both from an experimental and numerical modelling view point. Laboratory experiments have, however, only provided limited evidence of the nature of these secondary flows, mainly due to the intrinsic difficulties in the experimental instrumentation set-up to measure specific flow processes associated with cross-channel secondary circulations in rotating bi-directional stratified flows. Johnson and Ohlsen (1994) highlighted the development of cross-channel interfacial tilt associated with the geostrophic adjustment of rotating exchange flows in a semi-circular experimental channel, with the presence of bottom and

interfacial Ekman layers also demonstrated. Davies et al. (2006) investigated the cross-channel dynamics of a dense deep-water outflow using a rotational tank facility that incorporated idealised channel topography to represent the Faroe Bank Channel geometry downstream of the threshold sill. The cross-channel flow structure of the dense water overflow again suggested the dominance of Ekman dynamics, with an outward transverse flow and corresponding flow reversals at the bottom boundary and inclined interface. Similar results have also been obtained numerically by Cuthbertson et al. (2021) when considering the cross-channel flow structure of rotating exchange flows generated across a submerged rectangular sill. Here, Ekman boundary layers were also predicted to develop in the geostrophically-adjusted dense water layer at the horizontal sill boundary and at the inclined interface, with a compensatory interior flow in the opposite direction. Burchard et al. (2009) also investigated the transverse structure in the Western Baltic Sea (i.e. where a gravity current is developed) observing a characteristic lateral wedge-shaped density structure. The hydrodynamics of highly stratified estuaries, particularly associated with cross-channel or secondary flow circulations in bi-directional exchange flows, has also received considerable attention from both numerical and observational perspectives (e.g. Chant, 1997, 2010; Garrett, 2004; Lerczak and Geyer, 2004; Pein et al., 2018; Hosseini et al., 2023). Despite these contributions, secondary flow features for bi-directional stratified flows are not yet fully understood and require further in-depth analysis, as pointed out by Garrett (2004). For example, the flow structure of cross-channel or secondary circulations in the upper freshwater layer of a rotating, stratified exchange flow, and the variation in cross-channel flow dynamics along a sill-channel obstruction, have not yet been completely explored. Investigation of these secondary flows is a recognized point of interest to help estimate the dispersive nature of stratified exchange flows and determine the transport of substances to the shore (Chant, 2010). For non-rotational stratified exchange flows, while no experimental studies on the secondary flow structure within a trapezoidal channel have been found by the authors, several studies on homogeneous flows through straight channels provide valuable insights (e.g. Knight et al., 2007; Stoesser et al., 2015; Tominaga et al., 1989). In these cases, turbulent anisotropy is shown to generate secondary (cross-channel) circulations due to damping effect of turbulent fluctuations in the presence of the free surface, resulting in the formation of transverse flow cells that are dependant on the channel aspect ratio (i.e. width/height ratio). However, the nature of the secondary flow cell structures generated within bi-directional, stratified flows along a trapezoidal sill-channel, in the presence of both a density interface and a free surface, as well as the additional influence of rotation, have not investigated in any detail and remain largely unknown.

Based on the above review, the current study is focused on numerical model simulations of the large-scale experiments on rotating bi-directional stratified flows along a trapezoidal sill-channel, conducted by De Falco et al. (2021) at the LEGI Coriolis Platform in Grenoble. However, unlike De Falco et al. (2021), which focused primarily on the lateral distribution of the along-channel flow velocity and density fields, the main aim of these numerical simulations is to fully characterise the cross-channel, secondary flow circulations and their evolution under the different parametric conditions tested in De Falco et al. (2021). These conditions include (i) the effect of rotation (included as a Coriolis parameter), (ii) net-barotropic forcing of the bi-directional stratified flow (imposed saline and fresh water flow boundary conditions), and (iii) the evolution of hydraulic proprieties along the trapezoidal sill-channel obstruction. In respect of (i), the secondary flow structure of non-rotating, bi-directional stratified flows is also investigated to provide confidence in the consistency of the numerical simulations with secondary flows generated in experimental studies of bi-directional stratified flow in geometrically obstructed domains (e.g. Davies et al., 2002; Johnson and Ohlsen, 1994). It is noted, however, that these previous experimental studies do not provide quantitative data on the strength and magnitude of the secondary flow circulations. Within the

current study, we utilise the non-hydrostatic, s-coordinate Bergen Ocean Model (BOM) to simulate the laboratory scale experimental trapezoidal sill-channel configuration of De Falco et al. (2021). This enables the numerical investigation of the potential processes through which momentum can be transferred from the lower (saline) to the upper (fresh) fluid layers in bi-directional exchange flows generated through natural-shaped channels in both rotating and non-rotating frames of reference. This study therefore carries significant implications for both environmental and management issues in regions of restricted exchange (e.g. estuaries, sea straits and submarine oceanic channels), as elaborated in the discussion section of the paper. The BOM model is described in detail within Section 2 (Methods) of the current paper, with an appropriate validation of the numerical model simulations against experimental data from De Falco et al. (2021) presented in Section 3 (Results). Section 3 also presents descriptions of the along-channel and cross-channel flow structures for the numerical simulations in both rotational and non-rotational frames of reference. The implications (and limitations) of these results for full scale bi-directional stratified flows in estuaries and sea straits are then discussed in Section 4 (Discussion), including recommendations on the numerical model requirements for the study of secondary flow circulations (e.g. non-hydrostatic, vertical grid resolution, etc.). Also, the potential mechanism of substance transport from bottom waters to surface layer is discussed in detail. Finally, the main findings from the study are summarized in the conclusions (Section 5).

2. Methods

2.1. The numerical model and model set-up

In this numerical study, the non-hydrostatic version of the σ-coordinate Bergen Ocean Model (BOM) is applied to simulate dynamics of net-barotropic, stratified exchange flows through an idealised trapezoidal sill-channel. Application of the non-hydrostatic version of the model is most appropriate for steep topography obstruction in exchange flows (Lawrence, 1993). The capabilities of the non-hydrostatic version of BOM in laboratory scale studies have been previously demonstrated in Berntsen et al. (2009; 2016) and Cuthbertson et al. (2021).

Within the current study, the numerical simulations reproduce the large-scale, rotating exchange flow experiments of De Falco et al. (2021) conducted in the LEGI Coriolis rotating platform. Within the rotating tank facility, a submerged trapezoidal sill-channel topography was installed to model bi-directional exchange flows that are restricted in both their vertical and lateral (cross-channel) dimensions (Fig. 1). The geometry of the numerical domain emulates the physical trapezoidal sill-channel configuration characterized by $W_t = 2$ m (top width) and $W_b = 1$ m (bottom width), 45º side slopes, and a sill crest elevation of H_s

$= 0.5$ m above the basin bottom elevation (Fig. 1a). The total length of the horizontal sill-channel $L_s = 8.5$ m and both the exit and entrance slopes into the basins are 26.6º. The tank facility was filled with freshwater to an overall depth $H = 0.9$ m (equivalent to the depths in basins A and B), with a total sill-channel submergence depth $h_s = 0.4$ m. The only difference between the BOM computational grid and this experimental set-up is the extension of basin B (Fig. 1b) in the numerical simulations to ensure full development of the saline intrusion flow Q_2 prior to encountering the sill-channel topography to avoid spurious recirculations within basin B.

The BOM domain consists of a horizontal 0.1 m grid size (in both x and y dimensions, see Fig. 1b), with 161 equidistant σ-layers used in the vertical dimension (Fig. 2b). The high layer resolution in the z-direction is required to reproduce the sharp interfacial region between the counter-flowing dense saline water and the freshwater layers. The cell resolution in the lateral y-direction (i.e. equivalent to 20 grid cells across the trapezoidal channel, see Fig. 1b) was considered sufficient to enable accurate representation of the interfacial tilting and developing of secondary flow circulations across the sill-channel.

The initial configuration of the numerical experiments consisted of infilling the numerical domain with freshwater ($\rho_1 = 1000$ kg.m^{-3}) and imposing a saline water inflow ($Q_2 = 4.4$ l.s^{-1}) at the end boundary of basin B (Fig. 1a), which remained constant in all numerical simulations. The bi-directional exchange flows were then generated by imposing a counter-flowing freshwater flow Q_1 at the end boundary in basin A (Fig. 1a). The freshwater flow rate Q_1 was varied over a range of values to generate both uni- (i.e. $Q_1 = 0$ l.s^{-1}) and bi-directional exchange flows ($Q_1 > 0$ l.s^{-1}) with different net-barotropic forcing thus generated in the upper freshwater layer. Within the numerical experiments, a volume flux ratio, defined as $Q^* = Q_1/Q_2$ was kept constant over 1500 s before being gradually increased (i.e. through incremental steps in the Q_1 values) to a maximum value of $Q^* = 6$ over a total run duration of 4000 s or 160000 time steps (see Fig. 2a). Within all experimental runs (i.e. physical and numerical), the density excess $\Delta\rho$ of the saline water remained constant at 10 kg.m^{-3}. Note that a range of Q^* values tested in the numerical experiments was extended beyond that considered in the equivalent physical experiments, within which the maximum value of $Q^* = 4.5$ (see De Falco et al., 2021).

To ensure continuity within the numerical simulations, the prescribed saline water inflow volume flux Q_2 introduced near the bottom of the domain boundary in basin B was set equal to the prescribed lower layer outflow flux Q_2 at the bottom of the domain boundary in basin A (see Fig. 1a). Similarly, the inflowing freshwater volume flux Q_1 imposed near the surface at the domain boundary in basin A was also set equal to the prescribed upper layer outflow flux Q_1 at the top of the domain boundary in basin B (see Fig. 1a). The density of these outflowing water fluxes Q_1 and Q_2 at both sides of the model domain was set
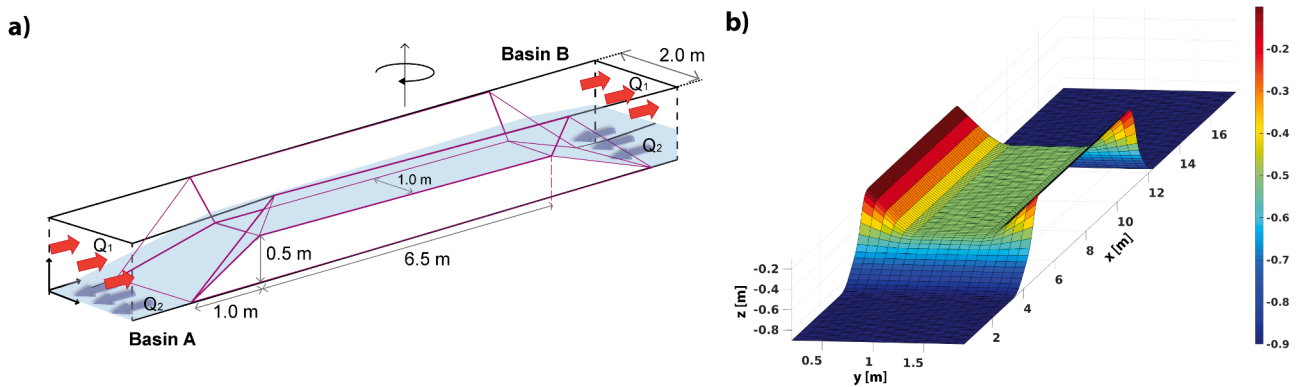

Fig. 1. (a) Schematic representation of the trapezoidal sill-channel, including the counter-flowing lower saline Q_2 and upper freshwater Q_1 fluid layers and main sill-channel dimensions. Basins A and B, for the inflow of freshwater and saline water, respectively, are also shown. (b) Numerical mesh used for the BOM simulations, including the (x,y,z) coordinate system used in the results presentation.
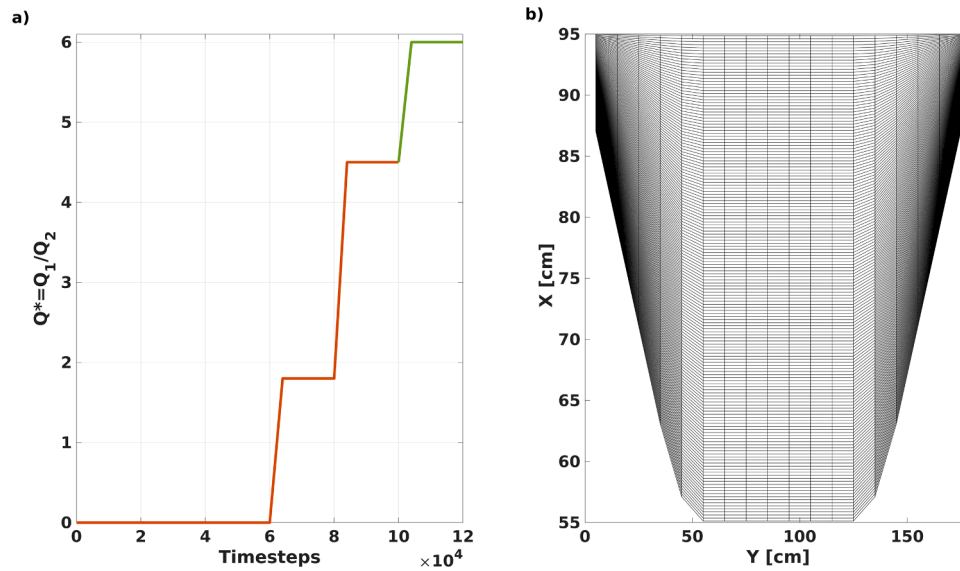
Fig. 2. (a) Incremental stepped increase in the volume flux ratio Q^* ($= Q_1/Q_2$) over duration for the BOM simulation with Q^* values equivalent to the experimental runs in De Falco et al. (2021) (shown in red) and the extended BOM simulation for higher Q^* values up to 6 (shown in green). (b) Details of the cross-channel computational σ-layer mesh (161 layers in vertical direction).

equal to the density of the ambient water immediately adjacent to these outflow regions. In addition, flow relaxation zones were added at both ends of the computational domain to smooth the inflows and outflows to and from the sill-channel-basin arrangement (Martinsen and Engedahl, 1987). In terms of the BOM computations, a mode-splitting technique was used with an external mode time step equal to 0.025 s, and a time step ratio between the external and internal mode (i.e. 3D and 2DH, respectively) computations set equal to 30, to ensure model stability.

The numerical experiments assumed constant horizontal viscosities (set equal to $5 \cdot 10^{-5}$ m^2.s^{-1}) and zero horizontal diffusivity. The standard Mellor-Yamada scheme (widely used in σ-layers models) was used to compute the vertical diffusivity and horizontal viscosity values, with a minimum value limitation to remove energy that flows towards and beyond the grid scale in order to avoid aliasing, while remaining small enough to allow the full representation of flow processes consistent with the grid resolution (Blumberg and Mellor 1987; Mellor and Yamada 1982). Sensitivity tests conducted with different turbulence schemes suggested limited effect on the nature of the modelled interfacial structure, with no turbulence model permitting the explicit representation of interfacial shear instabilities. The bottom boundary layer was parametrized using a quadratic relationship for the bottom stress with a drag coefficient equal to $2.5 \cdot 10^{-3}$. The bottom boundary model was not only applied to the horizontal bottom cells but also to lateral cells representing the frictional drag of the trapezoidal sloping side-walls. Sensitivity tests were also carried out applying different drag coefficients without substantial differences being observed on the mean dynamic exchange flow conditions modelled or the secondary flow circulations across the sill-channel.

The rotational effects were included numerically within the BOM simulations by the addition of the Coriolis acceleration applied in the clockwise direction, considering the geometric centre of the trapezoidal channel. The numerical experiments considered four different Coriolis parameter f values, indicative of increasing rotational effects [i.e. $f = 0$ (run S1), 0.06 rad.s^{-1} (S2), 0.1 rad.s^{-1} (S3) and 0.2 rad.s^{-1} (S4)], thus reproducing the same range of f values as tested in the large-scale rotating exchange flow experiments (De Falco et al., 2021). Dynamically, the effects of rotation on the bi-directional stratified flows through the trapezoidal sill-channel can be analysed using the Rossby number Ro, based on the saline intrusion layer, defined as

$$Ro = \overline{U_2}/f\overline{W} \tag{1}$$

where $\overline{U_2}$ is the cross-section averaged velocity in the lower saline layer, computed along the sill-channel length. $\overline{W}$ is the interfacial width of the dense saline outflow, which itself is function of the cross-section averaged thickness of the dense saline layer $\overline{h_2}$. This is also the length scale at which rotational effects become as important as inertial effects, as defined by the Rossby radius of deformation or baroclinic Rossby radius R, such that

$$R = \left(g' \cdot \overline{h_2}\right)^{0.5}/f \tag{2}$$

where $g' = g(\Delta\rho/\rho_1)$ is the reduced gravitational acceleration. The hydraulic regime of the dense saline layer through the sill-channel is also given by the densimetric Froude number Fr_2, of the form

$$Fr_2 = \overline{U_2}/\left(g' \cdot \overline{h_2}\right)^{0.5} \tag{3}$$

Finally, turbulent flow conditions are assured in all the experimental and numerical simulations as the Reynolds number $\overline{Re_2} = \overline{U_2} \cdot \overline{h_2}/\nu$ is of the order $O(10^4)$ (De Falco et al., 2021). A summary table of the main BOM simulations, including values for the main non-dimensional parameters is given in Table 1 [Note: these parameters are computed at the mid-point along the length of the trapezoidal sill-channel from numerical model outputs]. The Ekman boundary layers represent the length scale in rotating flows over which friction is important. In the current study, the turbulent nature of the bi-directional exchange flow suggests that the turbulent boundary (i.e. Ekman) layer thickness δ* can be estimated as (Weatherly and Martin, 1978),

$$\delta^* = 0.4 \cdot u^*/f \tag{4}$$

where u^* is a frictional (or shear) velocity estimated as $u^* = C_D^{1/2} \cdot U$, with C_D being the drag coefficient of the channel boundary and U the mean along-channel velocity in the lower saline water layer. Within the current study, typical values of Coriolis parameter $f = 0.1$ s^{-1} and $U = 0.05$ m.s^{-1}, with $C_D = 2.5 \cdot 10^{-3}$ (as above), implies that the turbulent Ekman boundary layers are of the order δ* = 0.01 m thick.

Table 1

Summary of BOM simulations performed. Non-dimensional parameters (Ro and Fr_2) and dimensional Rossby radius of deformation (R) computed from model simulation outputs midway along trapezoidal sill-channel. [(1)]No values for *Ro*, R or Fr_2 are provided for S4 at $Q* = 6$ a saline intrusion blockage conditions arise (i.e. $\overline{h_2}$ is equal to zero in the mid-point of the length of the channel).

Simulation	f (rad.s^{-1})	$Q*$ ($= Q_1/Q_2$)	Ro	R (m)	Fr_2
S1	0	0	–	–	0.20
		1.8	–	–	0.20
		4.5	–	–	0.20
		6	–	–	0.20
S2	0.06	0	0.32	1.93	0.21
		1.8	0.32	1.66	0.23
		4.5	0.29	1.58	0.22
		6	0.14	1.04	0.14
S3	0.1	0	0.28	1.99	0.18
		1.8	0.30	1.59	0.22
		4.5	0.25	1.52	0.19
		6	0.09	0.77	0.13
S4	0.2	0	0.15	0.80	0.20
		1.8	0.22	1.46	0.18
		4.5	0.14	1.17	0.13
		6	–[(1)]	–[(1)]	–[(1)]

3. Results

3.1. Numerical model validation: BOM simulation vs experimental data

For numerical model validation purposes, two set of experimental data from the study of De Falco et al. (2021), namely synoptic velocity fields obtained from Particle Image Velocimetry (PIV) measurements, and vertical density profiles from micro-conductivity probes, were used to validate the numerical simulations with three different flow ratios (i. e. $Q* = 0$, 1.8, 4.5), as detailed in Table 1. (Note: that the flow ratio $Q* = 6.0$ run in the extended BOM simulations was not conducted in laboratory tests).

Synoptic along-channel (*u*-component) velocity fields were obtained along the centreline of the trapezoidal channel for the cases S1 (i.e. non-rotational, $f = 0.0$ rad.s^{-1}), S2 and S4 (i.e. rotational, $f = 0.06$ rad.s^{-1} and 0.2 rad.s^{-1}, respectively) with $Q* = 0$, 1.8 and 4.5, as representative BOM simulation datasets for numerical validation. These BOM results have been compared with time-averaged PIV measurements obtained at the channel centreline close to the mid-point along the length of the trapezoidal sill-channel, with three separate PIV scans taken at this location over a duration of 30 s per scan and an interval of six minutes between individual scans (Fig. 3). As such, Fig. 3 shows the direct comparison between the numerical results from the BOM simulations and the three individual PIV scans for each of the selected model validation experiments. For the non-rotational case (S1, $Q* = 0$, 1.8, 4.5, Fig. 3), the numerical results show notable agreement with the three measured PIV scans at all $Q*$ values. Both the upper and lower layer velocity directions and magnitudes (i.e. positive velocities in the upper freshwater layer and negative velocities in the lower saline water layer) are well reproduced by the numerical model. A potential source of discrepancy may be associated with slight variations in location within the physical sill-channel domain where the measured PIV scans are compared directly to BOM velocity profiles obtained at a specific cell location within the model domain. In order to assess the quantitative agreement between the BOM simulation results and the experimental data, the skill score assessment index *SK* (Wilmott, 1981) and cost function χ (Holt et al., 2005) are used to validate the numerical model predictions, and are defined as
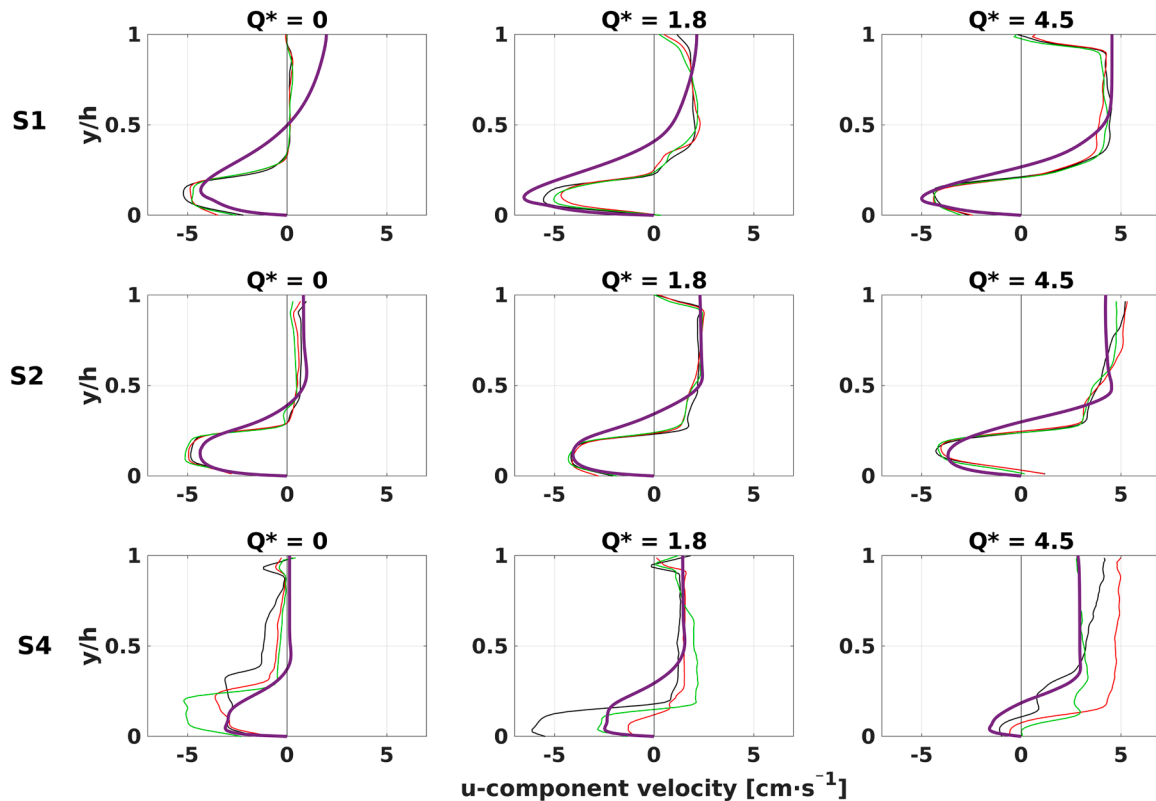

Fig. 3. Along channel (*u*-component) velocity profile comparisons between numerical simulations and experimental measurement for simulations S1, S2 and S4 (i.e. $f = 0$, 0.06 and 0.2 s^{-1}, respectively, see Table 1) and $Q*$ values shown. The thick purple profile corresponds to the BOM simulations, while the thinner (black, red and green) profiles correspond to the 3 separate PIV scans per run. Note: the instability shown in the measured PIV velocity structure for S4 (see De Falco et al., 2021) is not shown in the equivalent BOM numerical simulations.

$$SK = 1 - \frac{\sum_{i=1}^{n} (m_i - o_i)^2}{\sum_{i=1}^{n} (|m_i - \overline{o}| + |o_i - \overline{o}|)^2} \quad (5)$$

and

$$\chi^2 = \frac{1}{n \cdot \sigma_o^2} \sum_{i=1}^{n} (m_i - o_i)^2 \quad (6)$$

In Eqs. (5) and (6), *o* represents observational data, *m* represents the numerical modelling results, and *n* is the total number of data used in the comparison/validation, with the over bar (—) denoting mean values for observational data. Also, σ_o^2 is the variance of observations (square of standard deviation). In Eq. (5), a value of *SK* = 1 represents perfect agreement between model predictions and experimental observations occurs, while *SK* = 0 represents complete disagreement between model and observations. For the cost function χ [Eq. (6)], an acceptable predictive skill of the model is related to values lower than 1 (i.e. root-mean-square smaller than the standard deviation from observations), and a "well-modelled" variable threshold is situated at 0.4 (Holt et al., 2005). Table 2 shows the skill assessment between the measured and BOM-simulated exchange flow velocity profiles, presented in Fig. 3. In this regard, values of *SK* and χ indicate quantitatively a good agreement between experimental observations and BOM simulations, with 0.8 < *SK* < 1.0 and χ < 1.0, with some specific simulations regarded as "well-modelled" (i.e. χ < 0.4). In addition, the significant variability within the 3 PIV scans observed for the highly rotational case (i.e. run S4: $f = 0.2 \, s^{-1}$; Q* = 0, 1.8, 4.5; Fig. 3), as highlighted by De Falco et al. (2021), also coincides with a poorer skill assessment (i.e. lower *SK* and larger χ values for S4, Table 2) in comparison to runs S1 (i.e. $f = 0.0 \, s^{-1}$) and S2 (i.e. $f = 0.06 \, s^{-1}$). For this particular S4 run, the unsteady along-channel velocity structure originated in the lower dense layer, and is specifically associated with baroclinic instabilities that lead to the formation of large-scale eddies and a meandering propagation of the lower saline layer flow through the sill-channel. For this particular case, while the corresponding BOM numerical results tend to reproduce the main along-channel (u-component) velocity pattern in the upper and lower layers, they fail to represent the instabilities properly in space and time, leading to the poorer skill assessment (i.e. χ > 1 in S4 and Q* = 4.5).

Density profiles for the stratified flow conditions generated across the sill-channel were also measured by micro-conductivity probes, again located approximately at the midpoint along the length of the sill-channel [for details, see De Falco et al. (2021)]. BOM modelled data and observed profiles suggest two layer density structure along the sill-channel with the interfacial mixing layer shown to be relatively steeper in the experimental measurements in comparison to BOM numerical simulations. Fig. 4 shows the cross-channel variation in the elevation for $\rho* [= (\rho(z) - \rho_1)/\Delta\rho] = 0.5$ isopycnal. It is clearly shown that an increase of the Coriolis parameter *f* leads to an increase in interfacial tilting to the left hand side of the trapezoidal channel (looking in the direction of the saline water flow), consistent with the geostrophic

Table 2
Skill assessment between PIV-measurements and BOM-numerical simulations of the exchange flow velocity profiles shown in Fig. 3.

Simulation	f (rad·s^{-1})	Q* (= Q_1/Q_2)	SK	χ
S1	0	0	0.88	0.71
		1.8	0.90	0.70
		4.5	0.95	0.46
S2	0.06	0	0.98	0.28
		1.8	0.95	0.46
		4.5	0.96	0.27
S4	0.2	0	0.81	0.66
		1.8	0.86	0.70
		4.5	0.88	1.06

adjustment associated with clockwise Coriolis acceleration. While the degree of interfacial tilting from BOM computed and experimentally observed data are shown to be similar according to cross-channel elevation plots, particularly for the large Q* = 4.5 value (Fig. 4b), in some cases significant divergence arises between the experimental measurements and BOM simulations in the vertical position of the interface. This discrepancy is most likely to occur due the level of interfacial mixing within the experiments not being fully replicated in the numerical model simulations, as found previously in similar comparative studies (e.g. Cuthbertson et al., 2021). Overall, however, the cross-channel inclination of the $\rho* = 0.5$ interface, obtained in the current BOM simulations for rotating exchange flows, agree reasonably well with the corresponding experimental measurements by De Falco et al. (2021) and, in turn, lie close to the theoretical geostrophic slope $\alpha_g \approx f \cdot (\overline{u}_2 - \overline{u}_1)/g'$ that assumes the exchange flow is geostrophically balanced (i.e. transverse pressure gradient is balanced by the Coriolis acceleration - see De Falco et al. (2021) and Cuthbertson et al. (2021) for further discussion on this point).

In the context of interfacial mixing, De Falco et al. (2021) observed the formation of instabilities in the interface region (i.e. Kelvin-Helmholtz billows and Holmboe waves) that were systematically not possible to be reproduced in the BOM simulations (i.e. due to the RANS approximation). In addition, the horizontal grid resolution of 0.1 m was not sufficient to resolve the turbulent structures and entrainment processes occurring in the freshwater-saline interfacial layer, nor the additional mixing mechanics due to the friction effects of the trapezoidal sill-channel bottom and inclined side-walls. However, the BOM model is still deemed as capable of reproducing the transitional density profile from the lower saline to upper freshwater layers and the corresponding along-channel (u-component) velocity structure of these counter-flowing layers for a range of forcing conditions (i.e. Q* and *f* values).

3.2. Along-channel description of stratified exchange flow

The validated BOM numerical results for the non-rotating case (S1, Table 1) showed the development of bi-directional stratified (or exchange) flows at the mid-point along the trapezoidal sill-channel with an upper freshwater layer overriding a denser, counterflowing saline intrusion in the lower layer. However, as the model validation was limited to the central sill-channel region in which experimental measurements were obtained in De Falco et al. (2021), it is also important to understand how the structure of the exchange flow varies along the whole length of the sill-channel (i.e. from basin A to basin B) in both non-rotating and rotating frames of reference. In this regard, synoptic along-channel (u-component) velocity fields at the full centreline length of the sill-channel are shown in Fig. 5 for simulations S1 (i.e. non-rotating, $f = 0$ rad.s^{-1}) and S4 (i.e. rotating, $f = 0.2$ rad.s^{-1}) with Q* = 0, 1.8, 4.5 and 6 (i.e. also extended beyond the equivalent experimental data). Fig. 5 also shows the along-channel evolution of density profiles at three selected locations along the sill-channel (i.e. at *x* = 480 cm, 680 cm and 880 cm). For the non-rotational simulation (i.e. S1, Figs. 5a,c,e,g), the along-channel velocity fields show that when the imposed freshwater fluxes Q_1 is increased (i.e. increasing Q* values), the velocity at the upper layer also increases significantly. By contrast, the thickness h_2 of the saline lower layer (as defined by the *u* = 0 contour, plotted as a white isovel) decreases as a potential response of the increasing net-barotropic forcing from the upper freshwater layer. The along-channel velocity within the lower saline layer does not show a significant reduction for the simulations where Q* ≤ 4.5 (Figs. 5a,c,e), with the maximum lower layer velocity ~5 cm.s^{-1} at the mid-point of the sill-channel length. However, for Q* = 6 (Fig. 5 g), the upper freshwater flow becomes completely dominant, with h_2 reducing continually along the length of the sill-channel from basin B to A which, along with reduced velocities in the saline intrusion layer, is indicative of an arrested salt-wedge. In this latter case, the intensity of the upper
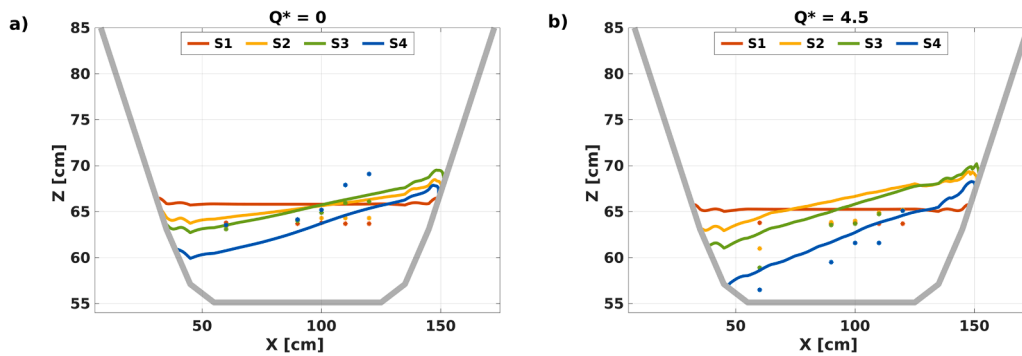
Fig. 4. Cross-channel elevation of the $\rho^* = 0.5$ isopycnal for simulations S1 – S4 (i.e. $f = 0$, 0.06, 0.1 and 0.2 s^{-1}, see Table 1) for (a) $Q^* = 0$ and (b) $Q^* = 4.5$. The continuous lines correspond to numerical results from the BOM simulations, while the data points refer to the experimental observations from micro-conductivity profiles.
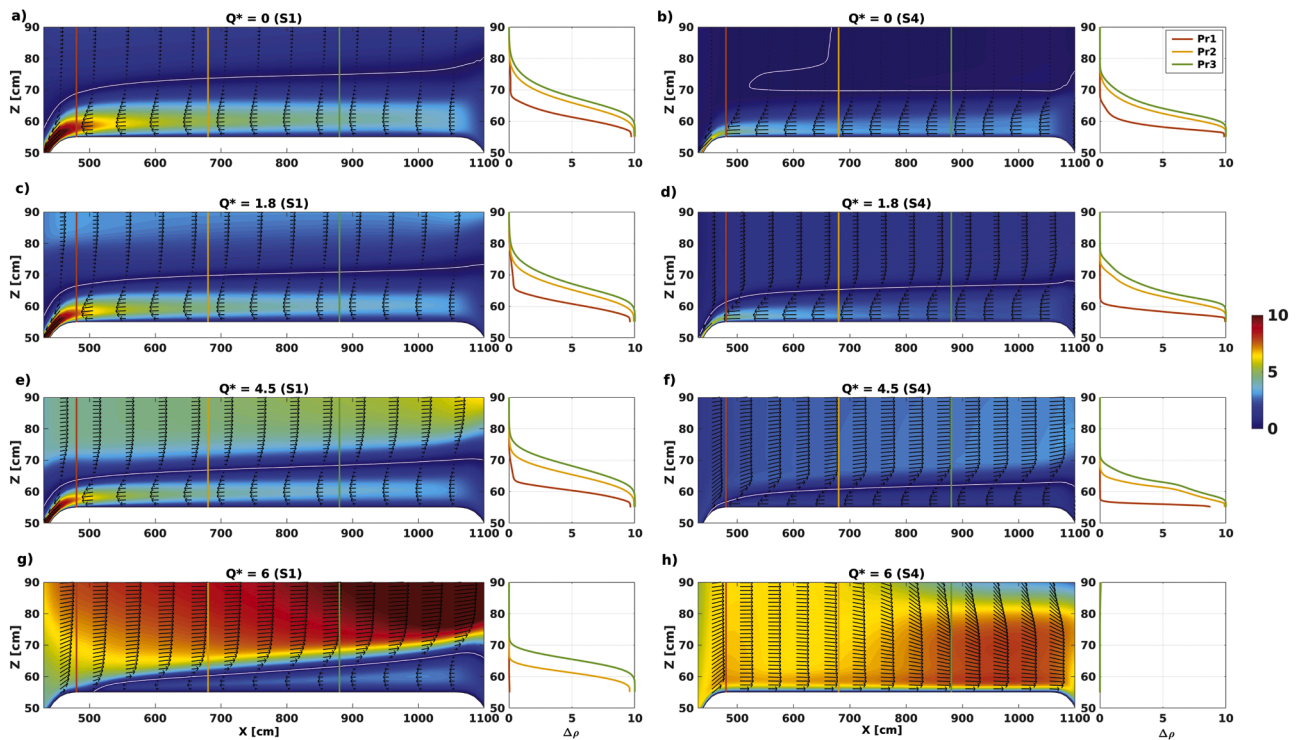

Fig. 5. Synoptic along-channel (*u*-component in cm.s^{-1}) velocity fields (left) and density excess profiles at three different sill-channel sections shown (right) for non-rotating (S1, $f = 0$ s^{-1}) and rotating (S4, $f = 0.2$ s^{-1}) cases (see Table 1). (a), (b) correspond to $Q^* = 0$; (c), (d) $Q^* = 1.8$; (e), (f) $Q^* = 4.5$; and (g), (h) $Q^* = 6$. The $u = 0$ velocity interface is also plotted in a white line.

freshwater flow prevents the intruding saline water across the sill-channel from spilling into basin A (i.e. full saline flow blockage). This is also confirmed by the corresponding density excess $\Delta\rho$ profiles, where at $x = 480$ cm a suppression of the saline water near the basin A (i.e. $\Delta\rho = 0$ throughout depth) is indicated. In this case, the saline layer blockage mechanism predicted by BOM has the characteristics of an arrested salt wedge, with a clear divergence of the $u = 0$ velocity isoline and the $\rho^* = [\rho(z) - \rho_1]/\Delta\rho = 0.5$ excess density isopycnal, in accordance with the salt wedge experiments of Sargent and Jirka, 1987. Indeed, for all the non-rotating cases (i.e. $Q^* \leq 6$), the density profiles exhibit asymmetry such that the $u = 0$ velocity interface is always located above the corresponding $\rho^* = 0.5$ density interface (see also Sargent and Jirka, 1987; Yonemitsu et al., 1996; Yang et al., 2019). The reduction in elevation of the $u = 0$ velocity interface along the sill-channel is suggestive of enhanced interfacial mixing induced by the increasing entrainment of the saline layer in the direction of dense water intrusion along the sill-channel (i.e. from basin B to A). An illustrative case of this

entrainment is shown for the $Q^* = 0$ case (Fig. 5a), where an induced freshwater counter-flowing is observed to form even when $Q_1 = 0$, proving substantial vertical mixing through the interface is reproduced by the numerical model. Similarly, the gradual reduction in the elevation of the $\rho^* = 0.5$ interface (i.e. for $x = 880$ cm → 680 cm → 480 cm) along the sill-channel (i.e. from basin B to basin A) suggests substantial entrainment of saline intrusion layer into the counterflowing upper freshwater layer.

The rotational simulations with increasing Q^* values (i.e. S4, Figs. 4b,d,f,h) are characterized by a marked reduction in the along-channel (*u*-component) velocities in both the lower (saline) and upper (fresh) layers, when compared directly to corresponding non-rotating cases (i.e. S1, Figs. 4a,c,e,g) at the centreline of the trapezoidal sill-channel cross-section. The rotational effects thus indicate that a cross-channel redistribution of the bi-directional exchange flows through the sill-channel occurs, as previously highlighted by the experimental measurements in the central sill-channel region [De Falco et al. (2021)].

Indeed, when considering this centreline section along the full length of the sill-channel, the clear reduction in the elevations of the $\rho^* = 0.5$ density interface are shown when compared directly with the corresponding non-rotational cases, due to this cross-channel redistribution of the saline layer. However, the rotational BOM results also clearly indicate a different relationship exists between the saline layer thickness h_2, velocity u_2 and Q^*, with increasing Q^* (i.e. increasing u_1) reducing the saline layer thickness h_2 and velocity u_2 at the centre line of the sill-channel. This suggests that the main along-channel saline layer intrusion has been displaced laterally away from the centreline of the trapezoidal sill-channel section. Indeed, at $Q^* = 6.0$, the saline water is displaced entirely from the channel centreline, with evidence of the upper freshwater layer only along the full length of the sill-channel (i.e. Fig. 5h).

In order to explore the effects of rotation on the bi-directional exchange flows generated along the sill-channel, the BOM simulation results are explicitly analysed for case S4 (see Table 1). As noted in the introductory section, the overall rotational effects related to Coriolis accelerations are expected to introduce geostrophic adjustment of internal fluid motions, with lateral tilting of the interface between the counter-flowing stratified flow layers. The main characteristics of the cross-channel density and velocity fields, most notably the geostrophic adjustment of the saline water intrusion at different cross-channel sections along the length of the sill-channel from basin B to basin A, is shown in Fig. 6 (i.e. looking from right to left). This non-symmetrical, cross-channel structure within the bi-directional stratified flow (with $Q^* = 4.5$) along the sill-channel is most clearly characterised by the tilting of the interface between the lower saline water and upper freshwater layers, while the representative thickness of the saline intrusion layer is also shown reduce along the sill-channel from basin B to basin A. This latter effect is shown to correspond to an increase in the maximum along-channel (*u*-component) velocity of the lower saline layer, particularly as the saline intrusion layer approaches the basin B end of the sill-crest (i.e. $x = 480$ cm). It is also interesting to note that the along-channel (*u*-component) velocity distribution in the counter-flowing, upper freshwater layer indicates that the largest velocities occur at the sloping side-walls of the trapezoidal sill-channel where there is no presence of underlying saline water.

The effect of this along-channel variability in the cross-channel, bi-directional stratified flow structure is considered in more detail in the next sections, particularly with respect to the secondary flow circulations generated laterally across the trapezoidal sill-channel, as well as being discussed in relation to real coastal, marine and oceanic contexts later in the discussion section (§4).

3.3. Secondary circulations in bi-directional, stratified flows

As well as the cross-channel distribution in the density and along-channel (*u*-component) velocity fields for the bi-directional exchange flows, the key aim of the numerical study was to investigate the lateral secondary flow circulations generated in the lower saline water and upper freshwater layers of the exchange flow through the trapezoidal sill-channel. As indicated within the introductory section, there remains a distinct lack of knowledge of these secondary flow structures generated within bi-directional, stratified flows, even though this has significant implications for the vertical transport of water masses, salinity, contaminants and nutrients within estuaries, tidal inlets and sea straits.

3.3.1. Non-rotational, bi-directional stratified flow

For the non-rotational BOM simulation (i.e. S1, Table 1), the lateral-vertical (*v*-, *w*-component) velocity vectors of the secondary flow circulations generated within the bi-directional, stratified flows for the range of flow ratios Q^* tested are shown in Fig. 7 (the associated colour scale being indicative of the vertical *w*-component velocity). Overall, common flow patterns are observed at the centreline of the trapezoidal channel, irrespective of the Q^* value, with upward flow within the upper fresh layer and downward flow within lower saline layer. The resulting lateral flow circulations are thus characterized by the presence of the density interface (shown as green isopycnals in Fig. 7) that, jointly with flow ratio Q^*, strongly influence the development of the closed secondary flow cells that form towards the lateral sloping sides of the trapezoidal channel in both the upper freshwater and lower saline water layers. Specifically, within the upper freshwater layer, two symmetrical, counter-rotating cells are observed to form (i.e. clockwise/anticlockwise at the right/left side of the channel) with upward flow in the centre of the channel and downward flow along the inclined channel side-walls. Preserving the continuity of flow in the interface, the lower saline layer is characterised by clockwise/anticlockwise cells in the left/right side of the channel side, leading to downward flow (i.e. downwelling) at the channel centre and upward flow (i.e. upwelling) at the bottom corners of the inclined channel side-walls. The overall strength of these secondary flow cells appears to be a function of the flow ratio Q^* as downward effects at the inclined side-walls are more intense for lower Q^* values, while secondary flows for higher Q^* values tend to be dominated by the positive vertical velocities in the centre of the trapezoidal channel cross-section (this effect is linked to the along-channel tilting of the interface and the "salt-wedge" blockage conditions shown in Fig. 5g).

The development of the upward (downward) flow regions at the centre of the upper (lower) layer and the formation of symmetrical,
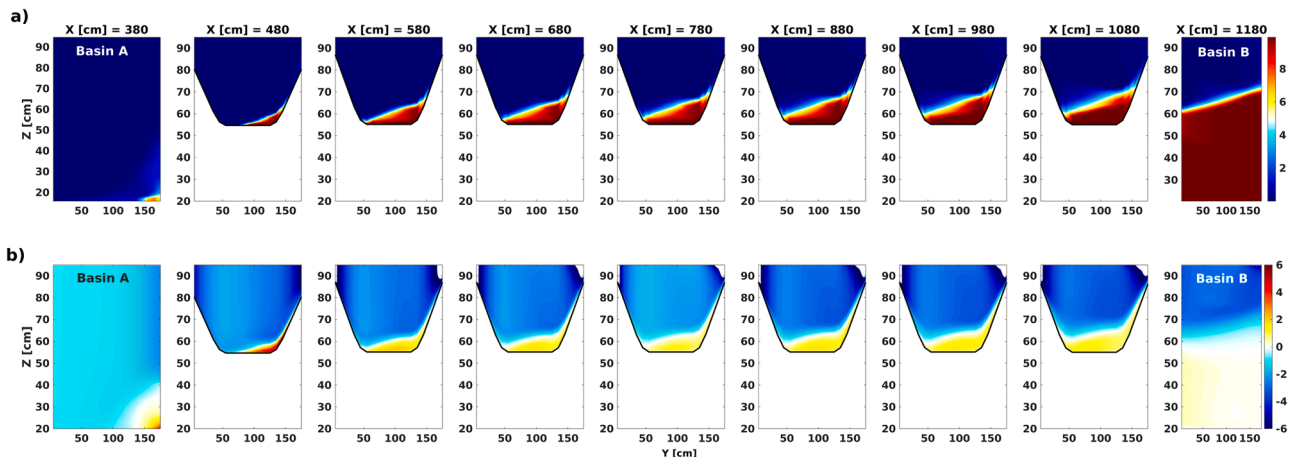

Fig. 6. BOM simulation results for case S4 ($f = 0.2 \ s^{-1}$) with $Q^* = 4.5$ (see Table 1) showing cross-channel variation in (a) density excess Dr (kg.m^{-3}) and (b) along-channel (*u*-component) velocity (cm·s^{-1}) fields at different along-channel (*x*) sill-channel locations between basins A and B.
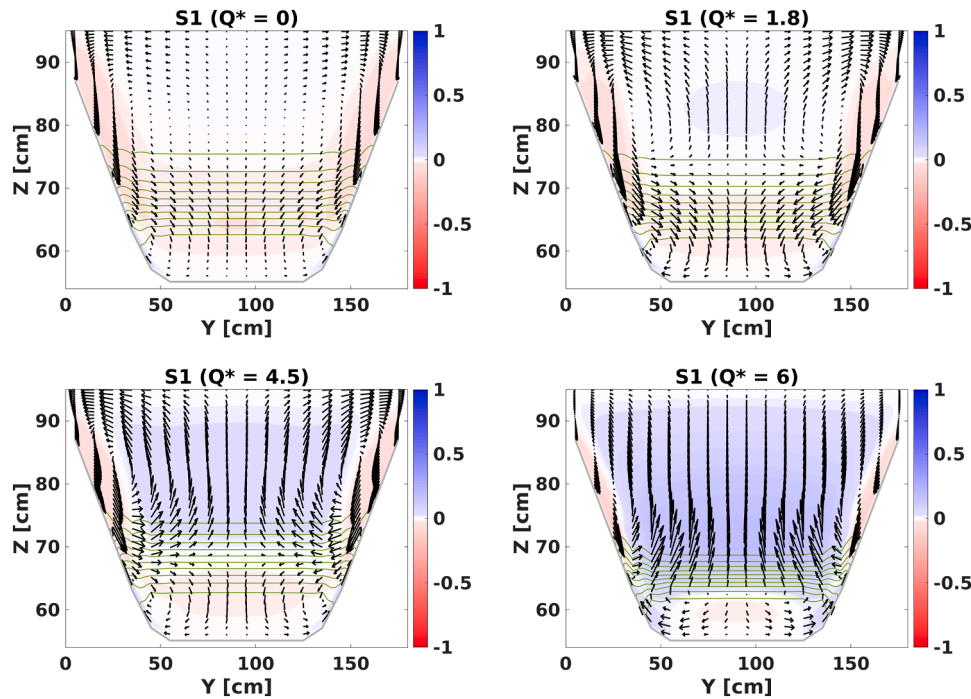
Fig. 7. Cross-channel (*v-*, *w*-component) velocity vector fields, vertical (*w*-component) velocity (cm.s^{-1}) colour map, and density isopycnals (green lines) for non-rotational case S1 (i.e. *f* = 0 s^{-1}, see Table 1) at computational mesh point *i* = 88 (i.e. *x* = 880 cm from origin) along the sill-channel for the *Q** values shown.

counter-rotating closed cells in both layers is a direct consequence of the anisotropy of turbulence, caused by the boundary conditions imposed at the horizontal bed, the inclined side-walls and the free surface, as demonstrated both experimentally and numerically by Tominaga et al. (1989) and Knight et al. (2007), respectively, for a homogeneous, uni-directional flow through a trapezoidal channel. In overcoming the inherent difficulty in measuring these secondary currents directly, Tominaga et al. (1989) observed that the secondary flow structure, characterised by the formation of two major flow cells in the upper corner of the inclined trapezoidal wall, were highly dependant of the channel aspect ratio. The structure of similar lateral secondary flow cells, observed by Knight et al. (2007) and Rhodes and Knight (1994), were also found to depend primarily on the trapezoidal channel aspect ratio (Knight and Patel, 1985). However, within numerical model simulations, the number and lateral distribution of secondary flow cells across a channel may also have had some dependence on the *y-z* grid resolution of the computational mesh, as indicated by Knight et al. (2007). In any case, these previous studies focussed on single layer, homogenous flows, while other lateral flow measurements in real channels (e.g. small estuaries) suggest that the magnitude of secondary flow velocities are of the order of 2–10 % of the primary mean flow velocity (e.g. Tominaga et al., 1989; Traykovski et al., 2007; Lerczak and Geyer, 2004)). For the bi-directional stratified flows considered in the current study, the presence of the internal boundary layer in the form of a density interface clearly adds significant complexity to the resulting secondary flow structure predicted within the counterflowing upper and lower fluid layers. In our case, the relative strength of the lateral circulations represents approximately 2–6 % of the maximum along-channel flow velocity in the lower saline layer (at *x* = 880 cm, see Fig. 5), therefore in broad agreement with the previous studies. It should also be noted that the formation of symmetrical, counter-rotating closed cells in the lower dense layer of the non-rotating exchange flows in the current study is also consistent with previous laboratory experiments of uni-directional gravity currents conducted in rectangular channels (e.g. Cossu et al., 2010; Davarpanah Jazi et al., 2020). These studies also displayed helicoidal flow cells that converge at the top and diverge at the bottom of the dense water gravity current through generation of two

adjacent cells spinning in opposite directions.

3.3.2. Rotational, bi-directional stratified flow

The lateral flow structure for the rotational BOM simulations is also characterized by different secondary flow circulations within the upper freshwater and lower saline water layers of the geostrophically-adjusted, bi-directional stratified flow. Specifically, the response of the exchange flow to rotation in terms of the transverse variation in the density structure, is characterized by the inclination of the density interface between the upper and lower layers, as already shown in Fig. 6. At the sloping side-walls, the isopycnals tend to tilt to perpendicular to the wall in order to satisfy the numerical condition of zero buoyancy flux at the boundaries (Lerczak and Geyer, 2004).

In terms of the corresponding secondary flow circulations within the counterflowing fresh and saline flow layers (also shown in Figs. 8 and 9), this first thing to note is the loss of symmetry within the flow cells generated in the upper and lower layers when compared to the non-rotating exchange flows (i.e. see Figs. 7 and 8 for a direct comparison with the same *Q** values). Indeed, within the lower saline water layer (beneath the inclined interface), the secondary cross-channel circulation is characterised by the development of bottom and interfacial Ekman layers. Evidence of these bottom Ekman layers is detected in BOM modelled rotating exchange flow experiments and are characterized by a thin boundary layer extending across the horizontal channel bottom, directed in the negative *y*-direction (i.e. from right to left looking downstream in direction of the saline flow). Overall, the Ekman layer thickness obtained numerically within the rotating BOM simulations is consistent with the theoretical values obtained by Eq. (4) [i.e. δ* = *O* (10^{-2}) m]. This bottom layer structure is shown in greater detail within Fig. 9d, along with the interfacial Ekman layer that is generated at the lower isopycnals within the inclined density interface in the same cross-channel direction as the boundary Ekman layer. The presence of this interfacial Ekman layer is only detected in certain runs. Furthermore, the interior flow within the lower saline intrusion layer is shown to be in the positive cross-channel *y*-direction, representative of the main sill intrusion flow being directed to the right (looking downstream in direction of the saline water flow) due to Coriolis acceleration, which acts
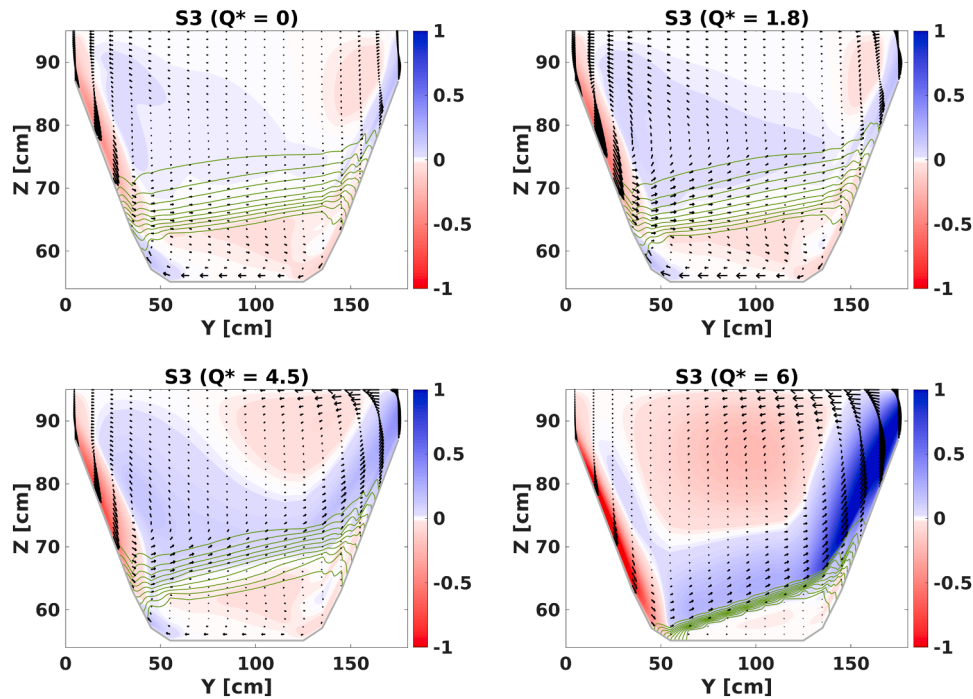
Fig. 8. Cross-channel (v-, w-component) velocity vector fields, vertical (w-component) velocity (cm.s^{-1}) colour map, and density isopycnals (green lines) for the rotational case S3 (i.e. $f = 0.1 \ s^{-1}$, see Table 1) at computational mesh point $i = 88$ (i.e. $x = 880$ cm from origin) along the sill-channel for the Q^* values shown.
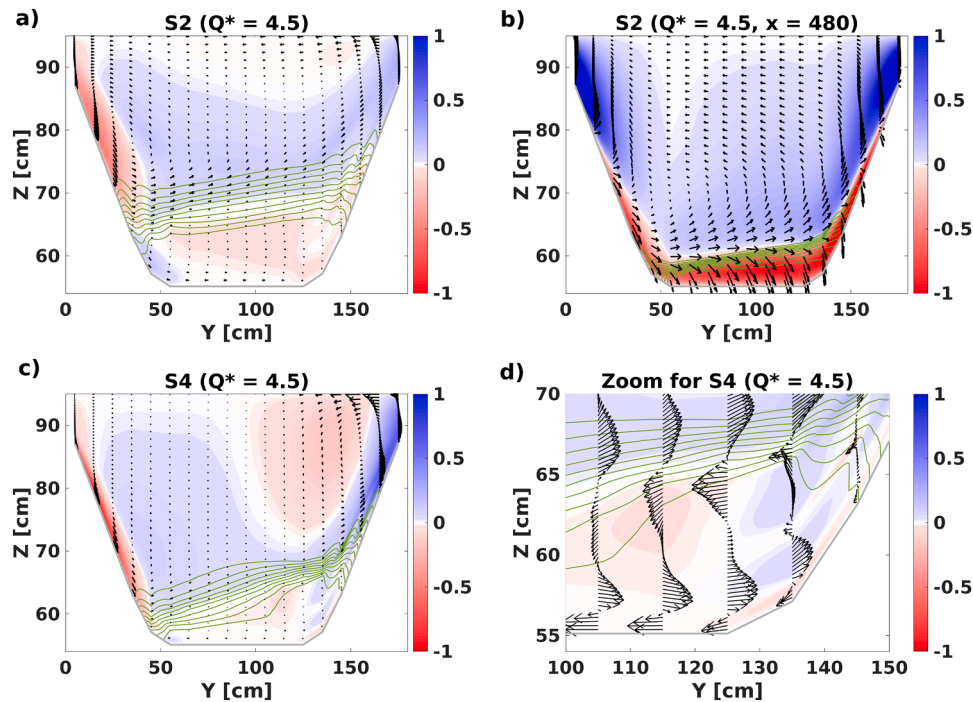

Fig. 9. Cross-channel (*v-*, *w*-component) velocity vector fields, vertical (*w*-component) velocity (cm.s^{-1}) colour map, and density isopycnals (green lines) for selected rotational cases S2 and S4 (i.e. $f = 0.06 \ s^{-1}$ and $0.2 \ s^{-1}$, respectively, see Table 1) with $Q^* = 4.5$ at computational mesh points (a) $i = 88$ (i.e. $x = 880$ cm from origin) (S2); (b) $i = 48$ (i.e. $x = 480$ cm from origin) (S2); and (c) $i = 88$ (i.e. $x = 880$ cm from origin) (S4). Subplot (d) provides enhanced detail on secondary flow structure in lower layer at $i = 88$ (i.e. $x = 880$ cm from origin) (S4) [i.e. zoomed region at bottom right of channel in subplot (c)].

as a volume balance to the boundary (and interfacial) Ekman layers.

The development of wedge-shaped, cross-channel density fields and the associated secondary circulations have been reported in both numerical and experimental simulations. Experimentally, qualitative similar secondary circulations have been observed in Johnson and Ohlsen (1994) for exchange flows within a rotating, semi-circular

channel, and in Davies et al. (2006) for a laboratory model of the dense deep-water outflow from the Faroe Bank channel, noting in both cases the geostrophic adjustment of the lower saline flow layer. Numerically, the secondary flow structure has been explored for gravity currents down submarine canyons in Berntsen et al. (2016) and for bi-directional, exchange flows across a rectangular sill in Cuthbertson

et al. (2021), both in a rotational frame of reference. However, limited information remains available on the characteristics of the secondary flow structure generated in the upper flow outside of the bottom dense water layer for rotating exchange flows. In the current study, the cross-channel flow field immediately above the inclined density interface is shown in Figs. 8 to be characterised by a flow in the positive *y*-direction that is also slightly upward in nature due to the tilting of the density interface. This upward flow is apparent in almost all of the rotational BOM simulations and provides continuity to relatively intense opposing flows experienced on the lateral slopes of the trapezoidal channel. In this context, a strong upward flow (i.e. upwelling) is observed to occur on the right side-slope, while a strong downward flow (i.e. downwelling) occurs on the left side-slope. These upwelling and downwelling flow regions are also observed to form in all the rotational BOM simulations (see Figs. 8, 9a and 9b), with their width and intensity (i.e. strength of vertical velocity) shown to depend on both the Coriolis parameter *f* and flow ratio Q^*.

In this regard, Fig. 10 shows the lateral transect of vertical velocities *w* at elevation $z = 80$ cm within the upper freshwater layer for all rotating and non-rotating exchange flow simulations and for the range of different Q^* and *f* values tested (see Table 1). For the non-rotational simulations (i.e. S1, $f = 0 \ s^{-1}$; Table 1), the vertical velocities for all Q^* values are shown to be considerably lower in magnitude when compared to equivalent rotational simulations (i.e. S2–4, $f = 0.06 - 0.2 \ s^{-1}$; Table 1), particularly towards the opposing inclined side-walls of the trapezoidal channel. It is also clear from these transects that increasing the rotational effects (i.e. by increasing the Coriolis *f* parameter between simulations S2 → S4, see Table 1) results in higher magnitude vertical velocities, again particularly intense at the inclined side-walls. The vertical water mass transport is also shown to increase when the flow ratio Q^* increases, consistent with the geostrophic balance when an increase of the along-channel flow induces an increase of the upward and downward flow (see transect evolution from $Q^* = 1.8 \rightarrow$

6). This indicates that the rotational effects introduce substantial lateral and vertical water mass transport, with upward and downward flow occurring at the right and left side of the trapezoidal channel, respectively. These vertical flow regions imply a clear analogy with surface waters being forced downwards and deep waters being forced upwards along the continental shelf and in open sea regions (i.e. due to downwelling and upwelling events), with the consequential influence in the vertical transport of substances and nutrients. The rotational effects on the generation of secondary flows requires the first order momentum balance being geostrophic (i.e. $f \cdot u = \partial p / \partial y$), even when the Rossby radius of deformation R is of the same order as the width of the trapezoidal channel (see Table 1). Chant (1997) noted that a misconception regarding estuarine circulations is that the effect of rotation is unimportant for small channels widths. In the current study, it is clear that the lateral-vertical flow intensity increases in response to an increase of the along-channel flow ratio Q^* (i.e. through an increase in upper freshwater flow Q_1). This acts to amplify the cross-channel velocity component (for a given Coriolis *f* parameter), which therefore tends to increase the interfacial tilting across the channel, producing higher lateral pressure gradients.

The secondary flow circulation pattern within the upper freshwater layer above the inclined interface is characterized by the gradual appearance of two large, closed flow cells as the Coriolis *f* parameter is increased [i.e. S2 → S4, $f = 0.06 - 0.2 \ s^{-1}$; Fig. 9(a) and (c)]. In contrast to the symmetrical, counter-rotating flow cells forming in the upper freshwater layer for the non-rotating exchange flows (Fig. 7), the equivalent upper layer flow cells for the rotating exchange flow are non-symmetrical, being consistent with the generation of upwelling and downwelling flow regions along the opposing side-slopes, as described above. Although qualitative descriptions of the secondary flow structure within the lower dense water layer of rotating exchange flows or unidirectional gravity currents have been provided in several contributions mentioned previously, the secondary flow circulations within the upper freshwater layer has not been described in detail before. A schematic diagram of these upper layer circulations was proposed by Johnson and Ohlsen (1994), and later reproduced by Garrett (2004), sketching qualitatively the anticipated secondary (cross-channel) circulation from their experimental observations. Ekman layer flows were plotted in the lower dense water layer, along with shear flow in the interfacial region, are in general in agreement with the secondary flow patterns obtained in our numerical BOM simulations. However, there remained significant uncertainty in terms of the interior water flow within the fresher upper layer [which in the schematic figures of Johnson and Ohlsen (1994) and Garrett (2004) was marked with a question mark]. In this regard, the co-rotating, non-symmetrical circulation cells provided by our numerical simulations provide a feasible and consistent description of the secondary flow dynamics of the interior of the upper freshwater layer, consistent with the shear flow in the interfacial region and the upwelling and downwelling flow regions at the opposing lateral slopes of the trapezoidal channel.

3.4. Variability in secondary flow circulations along the sill-channel

The secondary flow circulations for non-rotating and rotating exchange flows through a trapezoidal sill-channel have been shown to follow well-defined flow cell patterns, as a function of both the flow ratio Q^* and Coriolis *f* parameter, involving substantial regions of upward and downward flow in the upper freshwater layer. Figs. 5 and 6(b) also revealed the along- and cross-channel variations in the *u*-component velocity structure along the full length of the sill-channel. The expected feedback between the along-channel (*u*-component) velocities and secondary flow circulations has previously been observed in many real flow examples that are influenced by differential along-channel advection and/or geometrical constraints (e.g. Chant, 1997; MacCready and Geyer, 2010). Cuthbertson et al. (2018) identified the two key parameters for the along-sill variability in non-rotational exchange flows as (i)
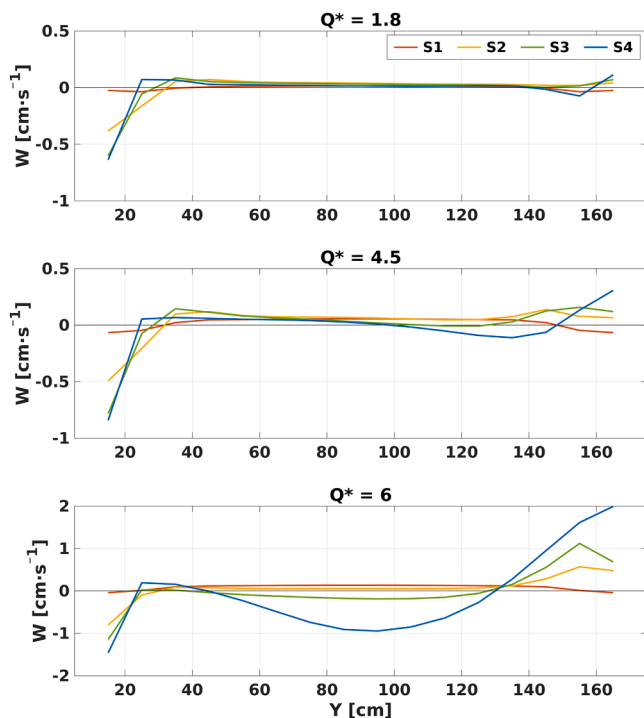

Fig. 10. Distribution of vertical (*w*-component) velocities (cm s^{-1}) along an in-channel, horizontal transect at $z = 80$ cm for the different Q* values shown in non-rotating (i.e. S1, $f = 0 \ s^{-1}$) and rotating (i.e. S2–S4, $f = 0.06$–$0.2 \ s^{-1}$) cases at computational mesh point $i = 88$ (i.e. $x = 880$ cm from the origin) along the sill-channel.

internal-flow head loss associated with boundary friction and interfacial shear, and (ii) mass exchange from the lower saline layer into the upper fresh layer due to entrainment. This also suggests that similar variability in the lateral flow structure may also be expected to occur in the trapezoidal sill-channel geometry under consideration in the current study, due to the specific constraining effects on the restricted exchange flow developing between basins A and B. For the rotational exchange flow cases in particular (i.e. S2 – S4, Table 1), the along-channel evolution of the laterally-distributed, wedge-shaped saline intrusion flow through the sill-channel has been highlighted in Fig. 6(a). In addition, the observed along- and cross-channel variability in the *u*-component velocity fields, shown in Figs. 5 and 6(b), suggest an evolving hydraulic flow regime in the along-channel direction between basins B and A, and particularly near the basin A end of the sill-channel [i.e. at $x = 480$ cm, Fig. 6(b)]. This evolving regime is shown by the variation in the densimetric Froude number Fr_2 (Eq. (3)) for the saline intrusion layer along the sill-channel (as shown in Fig. 11 for run S4 with $Q^* = 4.5$, $f = 0.2$ s^{-1}). Specifically, this indicates the significant increase in Fr_2 as the overspill into basin A is approached [i.e. due to the increase in cross-section averaged velocity $\overline{U_2}$ and corresponding reduction in cross-section averaged layer thickness $\overline{h_2}$ of the saline intrusion layer, as shown in Fig. 6(b) at $x = 480$ cm]. Similar along-channel variations in Fr_2 are also obtained for the other rotating (and non-rotating) exchange flow simulations conducted in the current study.

Indeed, direct comparison of Figs. 9(a) and (b) shows how this change in the along-channel velocity structure, especially within the lower saline intrusion layer, affects the secondary flows generated across the trapezoidal channel at two locations along the sill-channel (i.e. $x = 880$ cm and 480 cm, respectively) within the same rotating exchange flow simulation (i.e. S4, $Q^* = 4.5$, $f = 0.2$ s^{-1}; Table 1). In particular, the secondary flow circulations at the basin A end of the sill-channel [i.e. $x = 480$ cm, Fig. 9(b)] indicate no evidence of the Ekman layers found within the bottom saline water intrusion layer further along the sill-channel [i.e. $x = 880$ cm, Fig. 9(a)]. Furthermore, the secondary flow structure within the upper layer shows a dominance of upward flows close to basin A [i.e. $x = 480$ cm, Fig. 9(b)], with strong upwelling along the right side-slope and only a very thin boundary flow in the downward direction along the lower portion of the left side-slope. The associated co-rotating flow cells found within the upper flow layer [i.e. at $x = 880$ cm, Fig. 9(a)] are also shown to have diminished significantly at the basin A end of the sill-channel [i.e. $x = 480$ cm, Fig. 9(b)] due to the dominant upward flow velocities induced by the vertical and lateral constriction of the upper freshwater flow between basin A and the sill-channel.

4. Discussion and application to real channel systems

The BOM simulations conducted within this study have shown the effect of Coriolis accelerations on bi-directional, stratified flows led to geostrophic adjustment of internal fluid motions that, in turn, suppress turbulent mixing generated at the interface, and result in the development of Ekman boundary layers in the lower saline water layer through

Fig. 11. Along-channel evolution of the densimetric Froude number Fr_2 in the lower saline intrusion layer for rotational case S4 (i.e. $f = 0.2$ s^{-1}) with $Q^* = 4.5$. Sections A and B correspond to $x = 480$ and 880 cm from the origin of the model domain (i.e. at computational mesh points $i = 48$ and 88, respectively).

the trapezoidal sill channel. This is characterised both by a lateral "salt-wedge" distribution of the saline intrusion through the sill-channel and resulting cross-channel asymmetry in the induced secondary flow circulations. In our BOM numerical results, the rotational effects are first evidenced by the tilting of the density interface between the counter-flowing layers and the generation of lateral (or cross-channel) flows in upper and lower layer being consistent with previous studies of two layer flows (e.g. Cuthbertson et al., 2021; Davies et al., 2006; Johnson and Ohlsen, 1994; Umlauf et al., 2010) and gravity currents (Cossu and Wells, 2010; Davarpanah Jazi et al., 2020). Relating these findings with real exchange flow applications across submerged sills within fjords/estuaries and through sea straits, potential vortex cells generated within the upper and lower layers of the rotational cases shown in Figs. 8 and 9 appear able to lift up substances such as nutrients, low DO bottom waters, larvae or fine sediments in parcels of fluid that are homogeneous within the region of flow upwelling along the right side wall of the trapezoidal channel (looking in the direction of the lower saline intrusion flow). The importance of this vertical flux transfer from lower to upper flow layers may be relevant. Pumping up and down (i.e. upwelling and dowelling) may have substantial effects in semi-enclosed water bodies with limited water renewal such as in restricted tidal estuaries and silled fjords. Fine muds, silts and mine tailing wastes containing harmful chemicals are often dumped into deeper parts of estuaries and fjords under the assumption that these will not affect the water quality in the near surface region. In this sense, when the width of the estuaries and fjords are similar to, or greater than, the Rossby radius of deformation (normally in the order of a few km, see Inall and Gillibrand, 2010), the effects of the Earth's rotation may modify the nature of barotropic and baroclinic flows and induce potential vertical transport flows at the channel margins. The potential magnitudes of these vertical velocities across the idealised, scaled trapezoidal channel were shown previously in Fig. 9 for the range of conditions considered in the current study. This is extended in Fig. 12 to consider a horizontal section distributions of the vertical velocity (*w*-component), density excess ($\Delta\rho$) and the density excess vertical flux (i.e. $\Delta\rho \cdot w$) for a horizontal slice through the trapezoidal channel at $z = 85$ cm for runs S2 and S3 (i.e. $f = 0.06$ and 0.1 s^{-1}, with $Q^* = 4.5$, Table 1). This figure reveals that the density excess vertical flux $\Delta\rho \cdot w$ increases along the right channel margin as Coriolis f increases, consistent with the secondary flow structure in the upper layer and density interface tilting shown in the results section (Figs. 9 and 10). In this regard, the density excess flux may be conceived as being a generic substance or contaminant that can be transported upward from the bottom waters to the upper near surface flow layers, thus highlighting both the relevance and potential significance of these vertical transport effects at the channel margins. It should also be highlighted that these vertical transport mechanisms may act over extended periods (note that the BOM simulation times were only of the order of a few minutes), such that the time-integrated vertical transport from bottom layers to the surface over longer durations may be substantial and, thus, act as a significant vertical transport pathway for contaminants and pollutants through upwelling effects. Fig. 12 also shows distinct lateral variability of the flux upwelled at different locations along the trapezoidal channel due to the feedback between the along- and cross-channel flow dynamics. As a consequence, the geometrical restrictions of the trapezoidal channel (i.e. channel length, width, submergence depth and side wall inclination) may also have significant impacts on both the exchange flow dynamics through the channel and the associated vertical transport dynamics (i.e. upwelling and downwelling) along the channel margins, indicating the need for further BOM simulations to evaluate these effects.

The numerical results from the BOM simulations for bi-directional stratified flows through an idealized, constant-width, trapezoidal, sill-channel geometry have also correctly described the asymmetric secondary flow circulation structure generated within the lower dense water layer, consistent with previous experimental studies by Davies et al. (2006) and Johnson and Ohlsen (1994). Both these studies
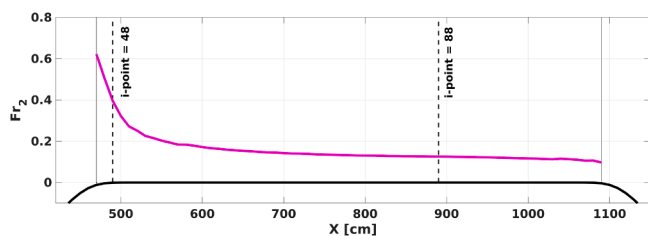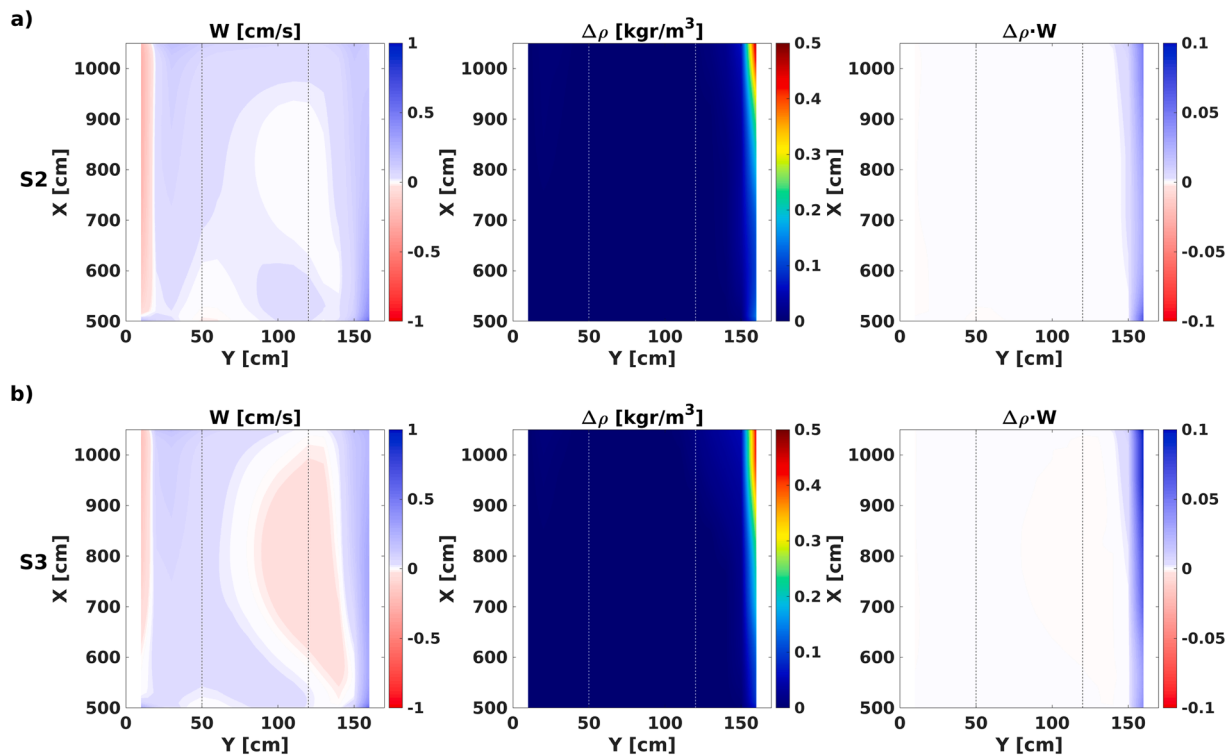
Fig. 12. 2D planform horizontal colourmaps at elevation $z = 85$ cm along trapezoidal sill-channel showing distribution of vertical (w-component) velocities, density excess ($\Delta\rho$) and density excess vertical flux (i.e. $\Delta\rho \cdot w$) for rotational cases (a) S2 (i.e. $f = 0.06$ s^{-1}) with $Q^* = 4.5$ (see Table 1) and (b) S3 (i.e. $f = 0.1$ s^{-1}) with $Q^* = 4.5$ (see Table 1). Note: the dotted vertical lines show the lateral extents of the horizontal channel bottom, while the right and left margins of the colormaps indicating show the intersection region of the horizontal slice at $z = 85$ cm with the inclined channel side walls.

demonstrated that the core of the dense water flow remains in geostrophic balance and a secondary circulation in the across-channel plane is maintained by the formation of Ekman layers and the bottom and interfacial boundaries. A similar complex secondary flow pattern is generated within the geostrophically-adjusted, lower saline intrusion flow along the trapezoidal sill-channel, which is shown to have a significant influence on the overall exchange flows dynamics. Indeed, when comparing the magnitude of the along-channel (u-component) velocity in the lower saline water layer for the non-rotational exchange flow [i.e. S1, $Q^* = 4.5$, $f = 0.0$ s^{-1}; Fig. 5(e)] and equivalent rotating exchange flow with the highest Coriolis f value [i.e. S4, $Q^* = 4.5$, $f = 0.2$ s^{-1}; Figs. 5(f) and 6(b)], the latter shows a considerable reduction in the overall saline intrusion flux through the sill-channel. As such, these idealised simulations may provide a good starting point for simulations of more varied sill-channel geometries and/or time-varying flow ratio Q^* (e.g. Faroe Bank Channel; Gibraltar Strait) where rotational effects are also significant. In this regard, the specification of a fixed Q* value or values is clearly not directly relevant to the simulation of exchange flow dynamics in naturally forced regions of restricted exchange, such as sea straits, estuaries and tidal inlets, where this flow ratio presents significant temporal variability (e.g. Lerzack and Geyer, 2004). In these real cases, a wide range of net-barotropic conditions would be expected to occur, where the exchange flow dynamics are either controlled by (i) tidal barotropic forcing [i.e. saline water intrusion dominates, Q* << 1 (e.g. Loch Etive, Scotland; Inall et al., 2004)], or (ii) a dominant freshwater outflow [i.e. Q* >> 1, (e.g. shallow-silled fjords with limited tidal intrusion; e.g. Bolstadfjord, Norway; Hamilton-Taylor, 1974).

The rotational effects on bi-directional exchange flows generated across a rectangular submerged sill has been previously addressed numerically using BOM in Cuthbertson et al. (2021). However, a systematic validation of this model was not possible for simulations conducted in a rotational frame of reference, due to a lack of experimental data on rotating exchange flows. This apparent disconnect between

numerical simulations and experimental validation has also been observed in similar previous studies that have either focussed solely on simplified numerical simulations (e.g. Berntsen et al., 2009; Umlauf et al., 2010) or on experimental measurements in rotating laboratory tank facilities (Davies et al., 2006; Cuthbertson et al., 2014, 2018; De Falco et al., 2021). Our contribution therefore focuses on the response of stratified exchange flows and nature of secondary flow circulations both within a rotational and non-rotational frame of reference, using a numerical model verified with experimental data provided in De Falco et al. (2021). This provides robustness to our analysis, with a coherent description of the secondary flow structure generated within bi-directional, stratified flows through an idealised topographic sill-channel constriction, complementing the previous experimental-based descriptions of Davies et al. (2006) and Johnson and Ohlsen (1994). Note that the mentioned numerical studies (e.g. Cuthbertson et al., 2021) do not provide a validation of the results in a rotational frame of reference using lab simulations data. Building on these previous studies, the current BOM simulations show that rotational effects initiate cross-channel secondary flow circulations, not only in the dense lower layer, but also in the upper freshwater layer, with two non-symmetric flow cells inducing substantial upwelling and downwelling at the opposing sides of the trapezoidal channel. Additionally, these BOM simulations build on the previous experimental work by De Falco et al. (2021) as they consider the evolution of the exchange flow structure (i.e. both velocity and density fields), the cross-channel secondary circulations and the hydraulic regime along the full length of the idealised sill-channel, rather than focusing on the central region where the experimental measurements were made.

One of the key characteristics of the numerical experiments is related to the high-resolution in the vertical direction, consisting of 161 σ-layers. In this regard, Haid et al. (2020) pointed out the need to establish sufficiently fine resolution for a proper description of lateral flows in straits (e.g. Danish Straits). The high numerical resolution of the

current BOM simulations has ensured appropriate representation of the along- and cross-channel titling of the density interface, details of the cross-channel variations in isopycnal structure, including isopycnal pinching/spreading and the required perpendicularity of isopycnals at the solid boundaries (i.e. sloping channel side walls) in order to satisfy the zero-buoyancy flux condition (Lerzack and Geyer, 2004). In addition, lateral distortion of the density isopycnals has been observed by several contributions (Umlauf and Arneborg (2009) and Johnson and Sandford (1992)), with a tendency for isopycnal pinching at one side spreading at the other side. This cross-channel feature has been observed partially by our simulations (e.g. S3 for $Q* = 6$, see Fig. 8) but non systematically due to the lack of spatial resolution in the y-direction. Furthermore, in terms of lateral flows, the non-rotational simulations indicate that vertical (downward) exchanges are intensified in a narrow band along the sloping side walls. In order to represent such lateral flow effects, the following considerations must be taken into account for the appropriate numerical reproduction of secondary flows: (i) a sufficiently high horizontal grid resolution, (ii) a suitable number of σ-layers in the vertical direction; and (iii) a non-hydrostatic modelling approach is required.

In relation to full-scale exchange flow simulations, most of the fjordic scale numerical studies, even those that perform well in terms of the main hydrodynamics processes (including matching the velocity and density structure) fail on all three of the conditions mentioned above (e. g. Dalsoren et al., 2020; Gillibrand and Amundrud, 2007; Asplin et al., 1999), and are thus likely to omit the main dynamics of the secondary flow circulations. It may also be added here that in ocean scale studies, the vertical flow scales are much smaller than the lateral scales and that, under such conditions, hydrostatic models can still produce averaged model (velocity and density) fields that are in good agreement with corresponding results from non-hydrostatic models [see, for instance, Hilt et al. (2020) and Sannino et al. (2014)]. However, in order to investigate overturning and rotary motion in secondary flow circulations, that is primarily targeted in the present study, a non-hydrostatic model with higher grid resolution both vertically and horizontally is required [see discussions in Afanasyev and Peltier (2001a,b); Farmer and Armi (2001); Berntsen et al. (2009)]. Even though we identify substantial vertical exchanges occurring within these secondary flows, our numerical analysis is possibly still lacking in terms of the horizontal resolution to permit a complete description of the full band-width of vertical flows occurring near to the walls. In this regard, and inspired by the apparent dependence of secondary flow cell structure on the channel width-to-height aspect ratio in non-rotational flow cases (e.g. Tominaga et al., 1989; Stoesser et al., 2015), future work in this area could include new BOM simulations taking into account the channel aspect ratio, channel shape and grid resolution to explore their dependence on the formation of lateral flow cells in rotational exchange flow cases.

Scientific modelling contributions on real straits, estuaries and tidal inlets have provided robust descriptions of exchange flow dynamics, while attempting to provide descriptions of the secondary flow structure (e.g. Chant, 1997; Lerzack and Geyer et al., 2004; Burchard et al., 2009). For example, Haid et al. (2020) attempted to solve the secondary circulation patterns in Danish strait through numerical modelling, suggesting a highly dependence of the resulting flow structure on the numerical mesh. In particular, they highlighted the secondary circulations to be rather complex due to phase of the inflow and outflow, the streamline geometry, and the along-axis location. Similarly, Stanev et al. (2018), in numerical simulations of exchange flow dynamics through Baltic Sea straits, showed strong and differing dependencies on net transport arising from time lags and differences between inflow and outflow conditions in individual straits. They also demonstrated the model's performance in resolving gravity flows and salinity structure to be dependant on grid resolution, particularly at narrower parts of the straits, but did not provide specific details of the cross-channel secondary flow structure of the exchange flows. More recently, Chen et al. (2023) explored the lateral momentum balance that drives the residual

flow on a cross-section in the German Bight, a predominantly well-mixed tidal inlet. In particular, the study investigated the role of ebb to flood tide asymmetries in creating secondary circulations, with advective accelerations found to be dominant in the lateral momentum budget during neap tides, driving an anti-clockwise secondary circulation (looking seaward). In contrast, the increased importance of covariance between eddy viscosity and vertical shear in the lateral momentum budget was found to reverse the secondary flow to a clockwise circulation during spring tides. In both cases, the contribution from Coriolis accelerations was found to be negligible compared to other forcing mechanisms.

Overall, the complexity of exchange flows through sea straits, tidal inlets and estuaries/fjords makes it difficult to obtain a perfect fit between observations and corresponding model outputs. However, future realistic model investigations in these coastal, marine and oceanic settings may benefit from the findings and conclusions, particularly on the structure of secondary circulations generated by non-rotating and rotating exchange flows through the straight, trapezoidal sill-channel considered in the current study. It is acknowledged that, while these idealised, laboratory scale numerical simulations clearly do not replicate perfectly the exchange flows in real settings, they provide valuable preliminary data and physical insights into important mechanisms associated with secondary flow, including upwelling and downwelling effects at the inclined channel boundaries. In this regard, the current numerical solutions can guide the development of more refined models, management strategies and practical solutions that take into account the intricacies and complexities of exchange flow dynamics in real coastal, marine and oceanic scenarios.

It is proposed that future work could include numerical simulations (and specific exchange flow experiments) focussed on resolving the near-wall dynamics, which will contribute to better understanding of the overall structure of secondary flows in bi-directional, stratified flows, and their impact on exchange flows dynamics (including flux transport of substances) across submerged sill topographies, through sea straits and narrows, and within stratified estuaries. In this sense, the geometry of the channel system (e.g. overall length, width-height ratio and cross-sectional shape), along with the topographic obstruction geometry (i.e. width and depth of flow constriction) would be expected to have a significant effect on secondary flow development and, hence, vertical flux transport (i.e. due to upwelling and downwelling at the channel margins), and therefore warrants further investigation.

5. Conclusions

The current study presents three-dimensional numerical simulations with the Bergen Ocean Model (BOM) that reproduce the main along-channel and cross-channel dynamic flow patterns of stratified exchange flows through the trapezoidal sill-channel in both rotating and non-rotating frames of reference. In this regard, Fig. 13 shows a simple schematic representation of the induced secondary circulations obtained from the numerical model simulations for these rotating and non-rotating exchange flows. The analyses focus on lateral (or secondary) flows conditions established in the sill-channel for different parametric conditions of the fresh-to-saline water flow ratio $Q*$ and the Coriolis parameter f (including the non-rotating exchange flow case where $f = 0.0 \ s^{-1}$). For the non-rotating exchange flow cases, the induced lateral secondary flow circulations suggest two differentiated flow cells systems with upward (downward) flow in the centre of the channel within the upper (lower) layer. The corresponding lateral secondary circulations in the rotating exchange flow cases are generally characterized by Ekman dynamics in the lower dense water layer (with isopycnal titling at the interface due to geostrophic adjustment) and two anti-clockwise cells in the upper freshwater layer (looking in the direction of saline water flow). With an increase in the Coriolis acceleration (i.e. increasing f) and the flow ratio $Q*$, vertical velocities at the inclined side-walls of the trapezoidal channel also increase in the upper layer. The resulting cross-
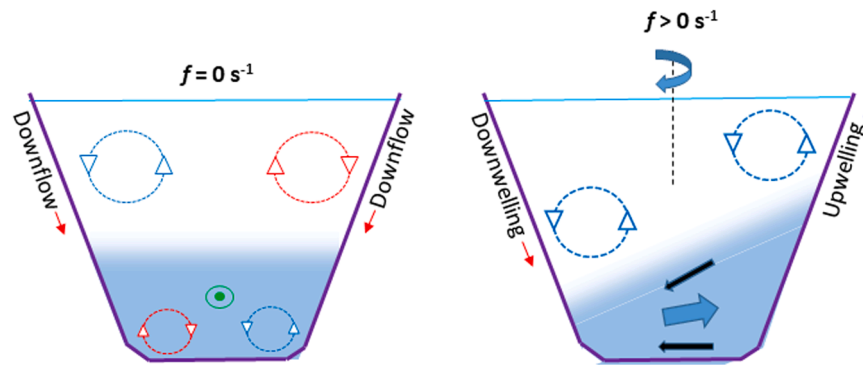
Fig. 13. Schematic representation of the secondary circulations obtained in a trapezoidal channel from the numerical simulations at the dense (blue) and freshwater (white) layers for (a) non-rotational (i.e. $f = 0$) and (b) rotational (i.e. $f > 0$ s^{-1}) exchange flows with $Q^* > 0$ (sketch is from the perspective of the saline intrusion flowing into the page). The figure also includes the frictional Ekman layers (black arrows) and the return flow (dark blue arrows) formed in the dense/lower layer for rotational exchange flows. Green arrow shows the downstream direction of the saltwater flow used in the analysis.

channel secondary circulation cells generated in the upper layer can induce vertical flux transport of deep water substances to the near-surface region through upwelling along the inclined side-slope of the channel, which has potential implications for nutrient and contaminant transport in exchange flow systems in real sea straits, tidal inlets and estuaries/fjords. Future works should therefore focus on extending simulations of the cross-channel secondary circulations in real exchange flow scenarios in over a wider range of geometrical restrictions and forcing conditions.

Declaration of Competing Interest

The authors declare the following financial interests/personal relationships which may be considered as potential competing interests:

Manel Grifoll reports administrative support was provided by Polytechnic University of Catalonia. Manel Grifoll reports a relationship with Polytechnic University of Catalonia that includes: employment.

Data availability

Data will be made available on request.

Acknowledgments

References

Afanasyev, Ya.D., Peltier, W.R., 2001a. On breaking internal waves over the sill in Knight Inlet. Proc. Roy. Soc. London A457, 2799–2825.

Afanasyev, Ya.D., Peltier, W.R., 2001b. Reply to comment on the paper "On breaking internal waves over the sill in Knight Inlet. Proc. Roy. Soc. London A457,, 2831–2834.

Asplin, L., Salvanes, A.G.V., Kristoffersen, J.B., 1999. Nonlocal wind-driven fjord-coast advection and its potential effect on plankton and fish recruitment. Fish Oceanogr. 8 (4), 255–263. https://doi.org/10.1046/j.1365-2419.1999.00109.x.

Berntsen, J., Xing, J., Davies, A.M., 2009. Numerical studies of flow over a sill: sensitivity of the non-hydrostatic effects to the grid size. Ocean Dyn. 59 (6), 1043–1059. https://doi.org/10.1007/s10236-009-0227-0.

Berntsen, J., Darelius, E., Avlesen, H., 2016. Gravity currents down canyons: effects of rotation. Ocean Dyn. 66 (10), 1353–1378. https://doi.org/10.1007/s10236-016-0981-8.

Blumberg, A.F., Mellor, G.L., 1987. A description of a three-dimensional coastal ocean circulation model. Coastal and Estuarine Sciences, Book 4. American Geophysical Union, pp. 1–16. https://doi.org/10.1029/co004p0001. *1-6.*

Borenäs, K., Lundberg, P., 2004. The Faroe-Bank channel deep-water overflow. Deep Sea Res. II Top. Stud. Oceanogr. 51 (4–5), 335–350. https://doi.org/10.1016/j.dsr2.2003.05.002.

Broadbridge, M., Toumi, R., 2015. The deep circulation of the Faroe-Shetland channel: opposing flows and topographic eddies. J. Geophys. Res. Oceans 120, 5983–5996. https://doi.org/10.1002/2015JC010833.

Bryden, H.L., Candela, J., Kinder, T.H., 1994. Exchange through the Strait of Gibraltar. Prog. Oceanogr. 33 (3), 201–248. https://doi.org/10.1016/0079-6611(94)90028-0.

Burchard, H., Janssen, F., Bolding, K., Umlauf, L., Rennau, H., 2009. Model simulations of dense bottom currents in the Western Baltic Sea. Cont. Shelf Res. 29 (1), 205–220. https://doi.org/10.1016/j.csr.2007.09.010.

Cerralbo, P., Grifoll, M., Espino, M., 2015. Hydrodynamic response in a microtidal and shallow bay under energetic wind and seiche episodes. J. Mar. Syst. 149 https://doi.org/10.1016/j.jmarsys.2015.04.003.

Chant, R.J., 1997. Secondary circulation in a highly stratified estuary. J. Geophys. Res. Oceans 102 (C10), 23207–23215. https://doi.org/10.1029/97JC00685.

Chant, R.J., 2010. Estuarine secondary circulation. A. Valle-Levinson (Ed.). Contemporary Issues in Estuarine Physics. Cambridge University Press, pp. 100–124. https://doi.org/10.1017/CBO9780511676567.006.

Chen, W., Jacob, B., Valle-Levinson, A., Stanev, E., Staneva, J., Badewien, T.H., 2023. Subtidal secondary circulation induced by eddy viscosity-velocity shear covariance in a predominantly well-mixed tidal inlet. Front. Mar. Sci. 10, 1105626 https://doi.org/10.3389/fmars.2023.1105626.

Cossu, R., Wells, M.G., 2010. Coriolis forces influence the secondary circulation of gravity currents flowing in large-scale sinuous submarine channel systems. Geophys. Res. Lett. 37 (17), 1–6. https://doi.org/10.1029/2010GL044296.

Cossu, R., Wells, M.G., Wåhlin, A.K., 2010. Influence of the Coriolis force on the velocity structure of gravity currents in straight submarine channel systems. J. Geophys. Res. 115, C11016. https://doi.org/10.1029/2010JC006208.

Cuthbertson, A., Davies, P., Stashchuk, N., Vlasenko, V., 2014. Model studies of dense water overflows in the Faroese channels topical collection on the 5th international workshop on modelling the ocean (IWMO) in Bergen, Norway 17-20 June 2013. Ocean Dyn. 64 (2), 273–292. https://doi.org/10.1007/s10236-013-0685-2.

Cuthbertson, A., Laanearu, J., Carr, M., Sommeria, J., Viboud, S., 2018. Blockage of saline intrusions in restricted, two-layer exchange flows across a submerged sill obstruction. Environ. Fluid Mech. 18 (1), 27–57. https://doi.org/10.1007/s10652-017-9523-2.

Cuthbertson, A., Berntsen, J., Laanearu, J., Asplin, M., 2021. Rotational effects on exchange flows across a submerged sill. Environ. Fluid Mech. 21 (2), 405–432. https://doi.org/10.1007/s10652-021-09779-5.

Dalsøren, S.B., Albretsen, J., Asplin, L., 2020. New validation method for hydrodynamic fjord models applied in the Hardangerfjord, Norway. Estuar Coast Shelf Sci. 246 (September) https://doi.org/10.1016/j.ecss.2020.107028.

Davarpanah Jazi, S., Wells, M.G., Peakall, J., Dorrell, R.M., Thomas, R.E., et al., 2020. Influence of Coriolis Force Upon Bottom Boundary Layers in a Large-Scale Gravity Current Experiment: Implications for Evolution of Sinuous Deep-Water Channel Systems. J. Geophys. Res. Oceans 125 (3). https://doi.org/10.1029/2019JC015284.

Davies, P.A., Guo, Y., Rotenberg, E., 2002. Laboratory model studies of Mediterranean outflow adjustment in the Gulf of Cadiz. Deep Sea Res. II Top. Stud. Oceanogr. 49 (19), 4207–4223. https://doi.org/10.1016/S0967-0645(02)00151-0.

Davies, P.A., Wåhlin, A.K., Guo, Y., 2006. Laboratory and analytical model studies of the Faroe Bank Channel deep-water outflow. J. Phys. Oceanogr. 36 (7), 1348–1364. https://doi.org/10.1175/JPO2917.1.

De Falco, M.C., Adduce, C., Cuthbertson, A., Negretti, M.E., Laanearu, J., Malcangio, D., Sommeria, J., 2021. Experimental study of uni- and bi-directional exchange flows in

a large-scale rotating trapezoidal channel. Phys. Fluids 33 (3). https://doi.org/10.1063/5.0039251.

Farmer, D., Armi, L., 2001. Stratified flow over topography: Models versus observations. Proc. Roy. Soc. London 457, 1–4.

Garrett, C., 2004. Frictional processes in straits. Deep Sea Res. II Top. Stud. Oceanogr. 51 (4–5), 393–410. https://doi.org/10.1016/j.dsr2.2003.10.005.

Gillibrand, P.A., Amundrud, T.L., 2007. A numerical study of the tidal circulation and buoyancy effects in a Scottish fjord: loch Torridon. J. Geophys. Res. Oceans 112 (5), 1–22. https://doi.org/10.1029/2006JC003806.

Haid, V., Stanev, E.V., Pein, J., Staneva, J., Chen, W., 2020. Secondary circulation in shallow ocean straits: observations and numerical modeling of the Danish Straits. Ocean Model. 148 (January), 101585 https://doi.org/10.1016/j.ocemod.2020.101585.

Hamilton-Taylor, J., 1974. The geochemistry of fiords of south-west Norway. Ph.D. thesis. University of Edinburgh, p. 138.

Hilt, M., Auclair, F., Benshila, R., Bordois, L., Capet, X., Debreu, L., et al., 2020. Numerical modelling of hydraulic control, solitary waves and primary instabilities in the Strait of Gibraltar. Ocean Model 151, 1–16.

Holt, J., Icarus Allen, J., Proctor, R., Gilbert, F., 2005. Error quantification of a high-resolution coupled hydrodynamic-ecosystem coastal-ocean model: part 1 model overview and assessment of the hydrodynamics. J. Mar. Syst. 57, 167–188.

Hosseini, S.T., Stanev, E., Pein, J., Valle-Levinson, A., Schrum, C., 2023. Longitudinal and lateral circulation and tidal impacts in salt-plug estuaries. Front. Mar. Sci. 10, 1152625 https://doi.org/10.3389/fmars.2023.1152625.

Inall, ME, Gillibrand, PA, 2010. The physics of mid-latitude fjords: a review. Geol. Soc. Lond. Spec. Publ. 344, 17–33. https://doi.org/10.1144/SP344.3.

Inall, M., Cottier, F., Griffiths, C., Rippeth, T., 2004. Sill dynamics and energy transformation in a jet fjord. Ocean Dyn. 54 (3–4), 307–314. https://doi.org/10.1007/s10236-003-0059-2.

Johnson, G., Ohlsen, D., 1994. Frictionally modified rotating hydraulic channel exchange and ocean outflows. J. Phys. Oceanogr. 24 (1), 66–78.

Johnson, G., Sandford, T., 1992. Secondary circulation in the Faroe bank channel outflow. J. Phys. Oceanogr. 22 (8), 927–933. https://www.ptonline.com/articles/how-to-get-better-mfi-results.

Knight, D., Patel, H., 1985. Boundary shear in smooth rectangular ducts. J. Hydraul. Eng. 111 (1), 29–47. https://doi.org/10.1061/(ASCE)0733-9429(1985)111:1(29).

Knight, D.W., Omran, M., Tang, X., 2007. Modeling depth-averaged velocity and boundary shear in trapezoidal channels with secondary flows. J. Hydraul. Eng. 133 (1), 39–47. https://doi.org/10.1061/(asce)0733-9429(2007)133:1(39).

Lerczak, J.A., Geyer, W.R., 2004. Modeling the lateral circulation in straight, stratified estuaries. J. Phys. Oceanogr. 34 (6), 1410–1428. https://doi.org/10.1175/1520-0485(2004)034<1410:MTLCIS>2.0.CO;2.

MacCready, P., Geyer, W.R., 2010. Advances in estuarine physics. Annu. Rev. Mar. Sci. 2 (1), 35–58. https://doi.org/10.1146/annurev-marine-120308-081015.

Martinsen, E.A., Engedahl, H., 1987. Implementation and testing of a lateral boundary scheme as an open boundary condition in a barotropic ocean model. Coastal Eng. 11 (5), 603–627. https://doi.org/10.1016/0378-3839(87)90028-7.

Mellor, G.L., Yamada, T., 1982. Development of a turbulence closure model for geophysical fluid problems. Rev. Geophys. 20 (4), 851–875. https://doi.org/10.1029/RG020i004p00851.

Ott, M.W., Dewey, R., Garrett, C., 2002. Reynolds stresses and secondary circulation in a stratified rotating shear flow. J. Phys. Oceanogr. 32 (11), 3249–3268. https://doi.org/10.1175/1520-0485(2002)032<3249:RSASCI>2.0.CO;2.

Papadakis, M.P., Chassignet, E.P., Hallberg, R.W., 2003. Numerical simulations of the Mediterranean sea outflow: impact of the entrainment parameterization in an isopycnic coordinate ocean model. Ocean Modell. 5 (4), 325–356. https://doi.org/10.1016/S1463-5003(02)00042-2.

Pein, J., Valle-Levinson, A., Stanev, E.V., 2018. Secondary circulation asymmetry in a meandering, partially stratified estuary. J. Geophys. Res. Oceans 123. https://doi.org/10.1002/2016JC012623.

Rabe, B., Smeed, D.A., Dalziel, S.B., Lane-Serff, G.F., 2007. Experimental studies of rotating exchange flow. Deep Sea Res. I Oceanogr. Res. Pap. 54 (2), 269–291. https://doi.org/10.1016/j.dsr.2006.11.002.

Rhodes, D., Knight, D.W., 1994. Distribution of shear force on boundary of smooth rectangular duct. J. Hydraul. Eng. 120 (7), 787–807. https://doi.org/10.1061/(ASCE)0733-9429(1994)120:7(787).

Sannino, G., Sánchez-Garrido, J.C., Liberti, L., Pratt, L., 2014. Exchange flow through the Strait of Gibraltar as simulated by a σ-Coordinate hydrostatic model and a zCoordinate nonhydrostatic model. In: Borzelli, G.L.B., Gačić, M., Lionello, P., Malanotte-Rizzoli, P. (Eds.), The Mediterranean Sea: Temporal Variability and Spatial Patterns, Geophysical Monograph 202. American Geophysical Union.

Sargent, F.E., Jirka, G.H., 1987. Experiments on saline wedge. J. hydraul. Eng. 113 (10), 1307–1323.

Seim, K.S., Fer, I, Berntsen, J., 2010. Regional simulations of the Faroe Bank Channel overflow using a σ-coordinate ocean model. Ocean Modell. 35 (1–2), 31–44. https://doi.org/10.1016/j.ocemod.2010.06.002.

Stashchuk, N., Vlasenko, V., Sherwin, T.J., 2011. Numerical investigation of deep water circulation in the Faroese channels. Deep Sea Res. I Oceanogr. Res. Pap. 58 (7), 787–799. https://doi.org/10.1016/j.dsr.2011.05.005.

Stoesser, T., McSherry, R., Fraga, B., 2015. Secondary currents and turbulence over a non-uniformly roughened open-channel bed. Water 7 (9), 4896–4913. https://doi.org/10.3390/w7094896 (Switzerland).

Tominaga, A., Nezu, I., Ezaki, K., Nakagawa, H., 1989. Structure turbulente à trois dimensions dans des écoulements à surface libre en canal rectiligne. J. Hydraul. Res. 27 (1), 149–173. https://doi.org/10.1080/00221688909499249.

Traykovski, P., Wiberg, P.L., Geyer, W.R., 2007. Observations and modeling of wave-supported sediment gravity flows on the Po prodelta and comparison to prior observations from the Eel shelf. Cont. Shelf Res. 27 (3–4), 375–399. https://doi.org/10.1016/j.csr.2005.07.008.

Umlauf, L., Arneborg, L., 2009. Dynamics of rotating shallow gravity currents passing through a channel. Part I: observation of transverse structure. J. Phys. Oceanogr. 39 (10), 2385–2401. https://doi.org/10.1175/2009JPO4159.1.

Umlauf, L., Arneborg, L., Hofmeister, R., Burchard, H., 2010. Entrainment in shallow rotating gravity currents: a modeling study. J. Phys. Oceanogr. 40 (8), 1819–1834. https://doi.org/10.1175/2010JPO4367.1.

Weatherly, G.L., Martin, P.J., 1978. On the structure and dynamics of the oceanic bottom boundary layer. J. Phys. Oceanogr. 8, 557–570.

Wilmott, C.J., 1981. On the validation of models. Phys. Geogr. 2, 184–194.

Yang, A.J.K., Tedford, E.W., Lawrence, G.A., 2019. The spatial evolution of velocity and density profiles in an arrested salt wedge. Theor. Appl. Mech. Lett. 9 (6), 403–408. https://doi.org/10.1016/j.taml.2019.06.005.

Yonemitsu, N., Swaters, G.E., Rajaratnam, N., Lawrence, G.A., 1996. Shear instabilities in arrested salt-wedge flows. Dyn. Atmos. Oceans 24 (1–4), 173–182. https://doi.org/10.1016/0377-0265(95)00444-0.